J. Fluid Mech. (2007), *vol.* 590, *pp.* 1–33. © 2007 Cambridge University Press
doi:10.1017/S0022112007007768 Printed in the United Kingdom

Stagnation-point flow under free-stream turbulence

ZHONGMIN XIONG† AND SANJIVA K. LELE
Department of Mechanical Engineering, Stanford University, Stanford, CA 94305, USA

(Received 7 May 2006 and in revised form 4 June 2007)

In this paper, the effects of free-stream turbulence on stagnation-point flow and heat transfer are investigated through large eddy simulation (LES) of homogeneous isotropic turbulence impinging upon an isothermal elliptical leading edge. Turbulent mean flow and Reynolds stress profiles along the stagnation streamline, where the mean flow is strain dominant, and at different downstream locations, where the mean flow gradually becomes shear-dominated, are used to characterize evolution of the free-stream turbulence. The Reynolds stress budgets are also obtained, and the turbulence anisotropy is analysed through the balance between the mean flow strain and the velocity pressure gradient correlation. In the presence of free-stream turbulence, intense quasi-streamwise vortices develop near the leading edge with a typical diameter of the order of the local boundary-layer thickness. These strong vortices cause the thermal fluxes to peak at a location much closer to the wall than that of the Reynolds stresses, resulting a greater sensitivity to free-stream turbulence for the heat transfer than the momentum transfer. The heat transfer enhancement obtained by the present LES agrees quantitatively with available experimental measurements. The present LES results are also used to examine the eddy viscosity and pressure-strain correlations in Reynolds stress turbulence models.

1. Introduction

Stagnation-point flow, where fluid approaching a solid surface divides into diverging streams, occurs ubiquitously in nature as well as in many engineering problems. An improved understanding of the stagnating flow turbulence and heat transfer is critical to a wide range of engineering applications, from protecting a gas turbine blade from being melted by the extremely hot and turbulent combustion gas, to enhancing the efficiency of a modern micro-electronics cooling system using micro-jet array impingement.

In his pioneering work, Hiemenz (1911) established that stagnation-point flow is one of the very few types that admit exact solutions of Navier–Stokes equations. Subsequent studies have been focused on understanding perturbed stagnation-point flows, i.e. the evolution and effects of various disturbances, including turbulence, that are present in the free stream. One of the prominent effects, first observed in the 1920s (Piercy & Richardson 1928, 1930), is that free-stream turbulence induces large heat transfer enhancement at the stagnation point (Giedt 1949; Hegge-Zijnen 1957; Kestin, Maeder & Sogin 1961). Various semi-empirical correlations have been proposed to quantify this effect, mostly based on the mean flow Reynolds number

† Present address: Lawrence Livermore National Laboratory, Livermore, CA, 94550, USA.

and the free-stream turbulence intensity (Smith & Kuethe 1966; Kestin & Wood 1971; Lowery & Vachon 1975; Mehendale, Han & Ou 1991), but they have met with limited success. Later, it was recognized that turbulence length scale played a critical role in determining the overall effects of free-stream turbulence. By incorporating turbulence length scale into the correlations, the applicability of prediction correlation is significantly improved (Ames & Moffat 1990; Dullenkopf & Mayle 1995; Van Fossen, Simoneau & Ching 1995). Although different definitions of length scale are used in these correlations, the heat transfer enhancement is found generally to increase with increasing Reynolds number and turbulence intensity, but decrease with increasing turbulence length scale.

Theoretical studies of the free-stream turbulence effects in stagnation-point flows have ranged from the mean flow unsteadiness, the linear/nonlinear instability, to the vortex stretching/amplification effects. Lighthill (1954) studied a pulsating mean flow around a cylindrical body and obtained the Stokes-layer correction, but no significant change in heat transfer was found. Similarly modulated stagnation point flows were also studied by Ishigaki (1970), Pedley (1972) and Merchant & Davis (1989), but with an emphasis on the skin friction. The linear stability analysis was initiated by Görtler (1955) and Hämmerlin (1955), further extended by Kestin & Wood (1970), and finally clarified by Wilson & Gladwell (1978). It has been shown that plane stagnation-point flow is always linearly stable to three-dimensional disturbances. For finite-amplitude disturbances, Lyell & Huerre (1985) showed that the flow can be destabilized if the level of the external two- or three-dimensional disturbances exceeds a threshold value. The linear instability for the more general attachment-line boundary-layer flow has also been investigated by Lin & Malik (1996) and Theofilis *et al.* (2003). Morkovin (1979) argued that the enhancement of heat transfer is more likely to be the result of a forced response to upstream disturbances than to any internal flow instability, a view advocated earlier by Sutera (1965) who analysed the amplification of incoming organized disturbances by mean strain, indicating the sensitivity of the heat transfer to vortical disturbances. For turbulence impinging on a circular cylinder with either very large or very small scales, Hunt (1973) obtained the behaviour of second-order turbulence statistics by using a generalized rapid distortion theory (RDT). Xiong & Lele (2004) showed that the critical parameter in determining the evolution of upstream three-dimensional disturbance is the ratio between the disturbance length scale and the Hiemenz boundary-layer thickness. Using numerical simulation of a swept Hiemenz boundary layer, Spalart (1989) found that, out of initial white-noise disturbances, the most unstable disturbance-mode is the one with the same similarity form as the mean Hiemenz flow, an assumption made in the stability analysis mentioned above. The flow structures induced by free-stream turbulence in a stagnation region were found to be qualitatively similar to those induced by upstream organized disturbances (Xiong & Lele 2001). Bae, Lele & Sung (2000) showed that different length scales generate quite different flow patterns and in turn different heat transfer responses in a plane stagnation-point flow. Although much progress has been made over the years, a complete understanding of the effects of free-stream disturbances, particularly turbulence, in stagnation-point flows has not been achieved.

The free-stream turbulence effects have also proved difficult to incorporate into engineering turbulence models. The one-equation model (e.g. Spalart & Allmaras 1992), while widely used and shown to be particularly successful in aerodynamic flows (Bardina, Huang & Coakley 1997; Wilcox 2001), does not explicitly account for the effects of free-stream turbulence. Standard two-equation models, e.g. the $k-\epsilon$ or $k-\omega$ model, when used in stagnation-point turbulent flows, badly overpredict the turbulent

kinetic energy and heat transfer – this is termed the 'stagnation-point anomaly' (Champion & Libby 1991, 1994; Durbin 1996). A fundamental difficulty with the two-equation models is that turbulence is assumed to be predominantely isotropic and in quasi-equilibrium. However, stagnating-flow turbulence can be strongly anisotropic because different components of the fluctuation velocity respond differently to the mean flow straining. Reynolds stress models provide the generality to account for the anisotropy of the turbulence explicitly. Im, Huh & Kim (2002) used three variants of the Reynolds stress model; the GL model (Gibson & Launder 1978); the GL-CL model (Craft, Graham & Launder 1993); and the SSG model (Speziale, Sarkar & Gatski 1991), to compute both the impinging and countercurrent stagnation flows. Although the predictions from these models were better than $k-\epsilon$ type models, all the models still severely overpredict the turbulence kinetic energy, and have large discrepancies in other Reynolds stress components when compared to experimental measurements. The problem stems from the overprediction of the energy production and the underprediction of the redistribution by the pressure–strain correlations. This uncertainty may be attributed to the difficulty in, and hence the lack of, detailed experimental measurements in the immediate vicinity of the leading edge.

In this study, we carry out LES of the impingement of free-stream turbulence upon an isothermal elliptical leading edge. To allow direct comparison with experimental results, the flow configuration and simulation parameters are taken to match the experiments by Van Fossen *et al.* (1995). The first goal of the present study is to gain an improved understanding of the evolution of stagnating-flow turbulence and the mechanism of the heat transfer enhancement. Secondly, the simulation is aimed to help to reduce some of the uncertainty in turbulence modelling for strain-dominated flows. The relative magnitudes and distributions of various turbulence quantities are obtained from the LES data. The present simulation shows that the largest change in the turbulence structure occurs in the immediate region of the leading edge. Thirdly, it is hoped that the present LES data may help the general development and calibration of turbulence models when turbulence anisotropy becomes strong.

The rest of the paper is organized as follows. The basic governing equations for the LES are given in § 2. The numerical methods and validation procedures are described in § 3, along with a blending scheme for generating free-stream turbulence. The main simulation results, including the mean flow profiles, turbulence intensity and Reynolds stress budget, are presented in § 4. In § 5, we summarize the results and give concluding remarks.

2. Navier–Stokes equation and SGS modelling

The flow configuration for the present LES is shown in figure 1 with both the laboratory coordinates (x, y, z) and the local surface coordinate (s, n, z) labelled. The mean flow is two-dimensional and the turbulence is assumed to be homogeneous in the spanwise direction z.

The governing equations for the LES of compressible turbulence are the filtered Navier–Stokes equations. With the dynamic subgrid stress (SGS) model for compressible flows (Moin *et al.* 1991), they are written as

$$\overline{\rho}_{,t} + (\overline{\rho}\tilde{u}_i)_{,i} = 0, \tag{2.1}$$

$$\overline{\rho}\tilde{u}_{i,t} + \overline{\rho}\tilde{u}_j\tilde{u}_{i,j} = -\overline{p}_{,i} + \frac{1}{Re}[(\tilde{\lambda}\tilde{u}_{j,j})_{,i} + (2\tilde{\mu}_T\tilde{S}_{ij})_{,j}], \tag{2.2}$$

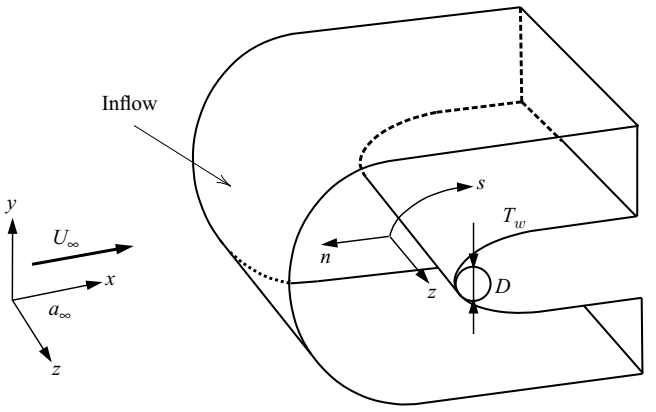

FIGURE 1. Flow configuration and inflow, outflow and wall boundary.

$$\overline{\rho}\tilde{T}_{,t} + \overline{\rho}\tilde{u}_i\tilde{T}_{,i} + (\gamma-1)\overline{\rho}\tilde{T}\tilde{u}_{j,j} = \frac{\gamma}{PrRe}[\tilde{\kappa}_T\tilde{T}_{,i}]_{,i} + \frac{\gamma(\gamma-1)M^2}{Re}[\tilde{\lambda}\tilde{S}_{ii}\tilde{S}_{jj} + 2\tilde{\mu}\tilde{S}_{ij}\tilde{S}_{ij}], \tag{2.3}$$

where

$$\overline{p} = \frac{\overline{\rho}\tilde{T}}{\gamma M^2} + \tfrac{2}{3}C_I\overline{\rho}\Delta^2|\tilde{S}|^2, \tag{2.4}$$

$$\tilde{\mu}_T = \tilde{\mu} + C\overline{\rho}\Delta^2|\tilde{S}|Re, \tag{2.5}$$

$$\tilde{\kappa}_T = \tilde{\kappa} + C\overline{\rho}\Delta^2|\tilde{S}|\frac{PrRe}{\gamma Pr_t}. \tag{2.6}$$

Here the tilde stands for Farve average; ρ is the density; u_i is the velocity vector, and T is the temperature. μ_T is the subgrid eddy viscosity. κ_T is the subgrid eddy thermal conductivity, and Pr_t is the turbulent Prandtl number. $S_{ij} = (u_{i,j} + u_{j,i})/2$ is the rate-of-strain tensor. M, Re are the mean flow Mach number and Reynolds number, and in the present study they are based on the upstream mean velocity U_∞, the speed of sound a_∞ and the leading-edge diameter D. $Pr = 0.7$ is the molecular Prandtl number and $\gamma = 1.4$ is the ratio of specific heats. The eddy coefficient C_I for the subgrid normal stress is set to zero and the turbulence Prandtl number Pr_t is set to unity. The eddy coefficient C for the subgrid shear stress is computed using the standard dynamic SGS model (see Xiong 2004 for details).

3. Numerical method

The numerical method and validation problems for the present LES are described briefly in this section. For more details, see Xiong (2004).

3.1. *Implicit scheme with linearized subiterations*

We first recast the compressible flow governing equations in a general form:

$$U_{,t} + F(U) = 0, \tag{3.1}$$

where $U = \{\rho, u, v, w, T\}^T$ is the vector of flow variables and $F(U)$ represents the nonlinear and viscous terms. Since for wall-bounded flows, explicit time integration schemes are prohibitively expensive because of the CFL stability constraint, in this

study we use an implicit dual-time-stepping scheme with linearized subiteration, which may be expressed as

$$\left[I + \frac{3\Delta\tau}{2\Delta t} I + \Delta\tau \mathscr{A}(U^n)\right] \Delta U^k = -\Delta\tau \mathscr{R}^k, \tag{3.2}$$

with

$$\mathscr{A} \equiv \frac{\partial F}{\partial U}, \quad \mathscr{R}^k = \frac{3U^k - 4U^n + U^{n-1}}{2\Delta t} + F(U^k), \quad \Delta U^k = U^{k+1} - U^k. \tag{3.3}$$

Here Δt is the physical time step, and $\Delta\tau$ is the pseudo time step for subiteration. At each physical time step, U^n is taken to be the initial value for U^k to start the subiteration at $k = 0$. If the subiteration converges, i.e. $\Delta U^k \to 0$, we obtain $U^{k+1} = U^k$. The final value of U^{k+1} is taken to be U^{n+1}, and $\mathscr{R}^{n+1} = 0$ recovers the second-order fully implicit scheme, which is unconditionally stable. Notice that instead of a function of U^k as in standard subiteration schemes, the left-hand side operator in (3.2) is only a function of U^n; therefore (3.2) is linear for variable ΔU^k. An LU decomposition of the coefficient matrices is performed at the first step of each subitereation, and the factored matrices are stored and used until the subiteration converges. This obviates the need for inverting the coefficient matrices at every subiteration step, and therefore significantly improves the subiteration efficiency.

3.2. *Spatial discretization*

At interior nodes, the five-point central difference scheme is used for first and second derivatives. Near the computational boundaries, five-point biased stencils are used. The resulting difference schemes are fourth- and third-order accurate for the first and second derivatives, respectively. Owing to the intrinsic non-dissipative nature, central difference schemes are often subject to the so-called two-δ wave instability caused by the decoupling of the even and odd grid points. In the LES context, we should not expect that a physics-based SGS model will automatically suppress such an instability. As well as the SGS model itself often being implemented with the same central difference scheme, the length scale of the two-δ waves is much shorter than that of the SGS model. The purpose of the SGS model is to extract energy at a correct rate at a cutoff scale – the scale at which the discrete representation becomes inadequate – and, for a grid spacing h, this is typically around a wavenumber of $hk \sim \pi/2$. However, for the two-δ wave, it occurs at the Nyquist wavenumber $hk \sim \pi$. Hence to suppress the two-δ waves, appropriate numerical damping procedures must be applied. In the present simulations, we choose the following fourth-order dissipation

$$D_n = -\epsilon_d \left(\Delta_\xi^4 \frac{\partial^4 U}{\partial \xi^4} + \Delta_\eta^4 \frac{\partial^4 U}{\partial \eta^4} + \Delta_z^4 \frac{\partial^4 U}{\partial z^4} \right), \tag{3.4}$$

where ϵ_d is the amplitude of the dissipation, and Δ_ξ, Δ_η and Δ_z are the grid spacing in the streamwise, normal and spanwise directions in computational space. Care must be taken to ensure that the added numerical dissipation is minimal and does not deteriorate the resolved solution. For this purpose, ϵ_d is chosen to be such that the magnitude of D_n is significantly smaller than the truncation error of the difference schemes. Based on modified wavenumber analysis, this may be achieved by requiring $\epsilon_d \leqslant 0.01 N_g$, where $N_g = (N_\xi + N_\eta + N_z)/3$ is the average number of grid points in one spatial direction. The resulting D_n is one order of magnitude lower than the truncation error and its effects on the results of the present LES are expected to be negligible. A more detailed discussion of the method and the demonstration of its effectiveness can be found in Xiong (2004).

3.3. *Boundary conditions*

Boundary conditions are introduced to replace the governing equations at the inflow, outflow and the wall boundaries of the computational domain. Consider an arbitrary boundary constraint at time level $n+1$ on the flow variable $U=\{\rho, u, v, w, T\}^T$

$$\mathscr{B}(U^{n+1})=0. \tag{3.5}$$

The general implicit treatment of the boundary conditions, in terms of the variable $\delta U = U^{n+1} - U^n$, can be written as

$$\left(\frac{\partial \mathscr{B}}{\partial U}\right)^n \delta U = -\mathscr{B}(U^n). \tag{3.6}$$

The boundary condition at the inflow provides the upstream mean flow information and also introduces free-stream disturbances or turbulence into the computational domain. For a subsonic inflow, characteristic analysis shows that four incoming quantities must be specified along with one outgoing quantity computed from the interior domain. The specific choice of these quantities depends on the formulation of the problem. In this study, we constrain the entropy, spanwise and tangential velocities, and the incoming Riemann invariant. The outgoing Riemann invariant is computed by first-order extrapolation from the interior points close to the boundary.

At the outflow, the parabolized Navier–Stokes equations is used following Collis (1997), i.e. the streamwise second-order derivatives in the equations are neglected. In addition, the pressure gradient at the outflow is obtained from the corresponding potential flow solution. This treatment has been shown to yield adequate and stable outflow boundary conditions both for the laminar and turbulent flow computations. No slip and isothermal conditions are applied at the wall for the velocities and temperature, and the periodicity condition is imposed in the spanwise direction.

Prior to turbulence simulations, the code is first validated on problems of laminar compressible boundary layer at a leading edge. The velocity and temperature profiles are compared with analytic self-similar solutions. A leading-edge acoustic receptivity problem is also computed and compared with previous numerical studies. These validation results are summarized in Appendix A.

3.4. *Generation of free-stream turbulence*

In this section, we describe a blending procedure combining independent, but statistically equivalent realizations of homogeneous isotropic turbulence into a unified turbulent flow field which serves as a realistic representation of free-stream turbulence. Consider two such turbulence fields, $U^{(1)}$ and $U^{(2)}$, that must be concatenated in the x-direction. We introduce a blending zone, extending from the interface into each of the fields by a short distance, and a linear combination

$$\boldsymbol{u} = \boldsymbol{u}^{(1)} \cos\theta + \boldsymbol{u}^{(2)} \sin\theta, \tag{3.7}$$

where θ varies smoothly from 0 to $\pi/2$ across the blending zone. The new field varies smoothly from one field to another and retains the mean values and second-order statistics of the original fields. The dependence of θ on x within the blending zone introduces an extra dilatation field, but it can be removed by using the Helmholtz decomposition theorem for the velocity vector. In figure 2, we plot the energy spectra of two original and the blended turbulence fields. It can be seen that the energy spectrum of the blended field remains essentially the same as the originals. A very small amount of energy is present at the lowest wavenumber owing to the increased

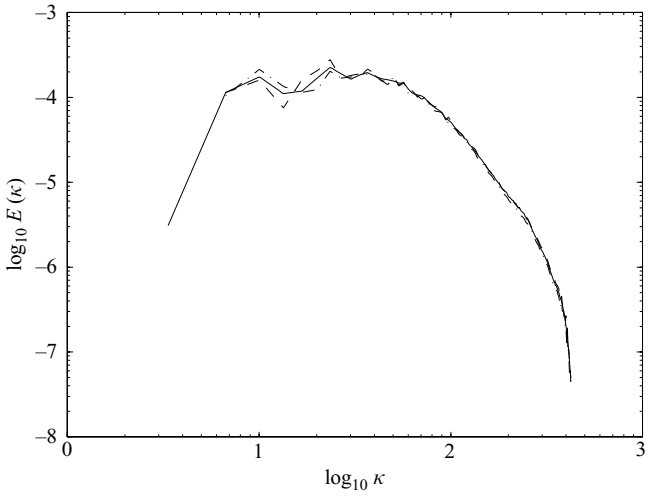

FIGURE 2. Energy spectra for the original and blended data sets. —·—, data 1; - - -, data 2; ——, blended.

length in the x-direction. More comparisons of energy spectra, as well as other quantities of interest, can be found in Xiong *et al.* (2004).

In the present LES, twelve realizations of such independent, but statistically identical homogeneous isotropic turbulence fields are pre-computed using LES with the same dynamic SGS model. To keep the same spanwise domain size as in the main LES, these simulations are carried out in a rectangular box of size $1.6D$, $1.6D$ and $0.4D$ in the x-, y- and z-directions, respectively. A $128 \times 128 \times 32$ grid is chosen to ensure the isotropy of the resulting turbulence. The code is adapted from a DNS code (Lui 2003) which uses a sixth-order compact finite- differencing scheme and a fourth-order Runge–Kutta time integration. Once the twelve turbulence fields are obtained, they are lined up spatially and joined together at the interfaces by applying the above blending procedure. The resulting turbulence field, twelve times longer than each individual realization, but with the same characteristics, serves as the free-stream turbulence, which will be convected into the computational domain through the inflow boundary.

4. LES results

4.1. *Simulation conditions*

The flow condition for the present LES is taken from the wind tunnel experiments by Van Fossen *et al.* (1995), and specifically, corresponding to the data set 244. In the experiments, free-stream turbulence is generated by placing a turbulence-generating grid upstream of a leading-edge model. The shape of the leading edge is a half-ellipse and the aspect ratio (length ratio between the major and minor axis) is 3 for this data set. Different values of turbulence intensity and length scale are obtained by varying the mesh size of the grid and its location relative to the leading edge. The model is kept at a constant temperature, and the heat transfer rate is measured in the stagnation-point region. The mean flow and free-stream turbulence parameters are summarized in table 1. The mean flow Reynolds number $Re_D = U_\infty D/\nu$ is based on far upstream incoming velocity U_∞ and the leading-edge diameter of curvature D. $M_\infty = U_\infty/a_\infty$ is the mean flow Mach number based on the sound speed a_∞ far upstream. Tu and L are the free-stream turbulence intensity and integral length

Re_D	M_∞	Tu	L/D	Re_L	Re_T	T_w/T_0	Domain (x, y, z)	$N_x \times N_y \times N_z$
42 000	0.15	0.05	0.1	210	93	1.075	$(3.5D, 5D, 0.4D)$	$191 \times 144 \times 48$

TABLE 1. Parameters of the mean flow and free-stream turbulence for the present LES.

scale; they are determined at the location of the leading edge, but in the absence of the model. The numerical procedure for determining L from the auto-correlation measurements is given in Van Fossen *et al.* (1995) and applied in the present LES. $Re_L = TuL/\nu$ is the Reynolds number based on integral length scale and turbulence intensity and the Re_T is the Taylor microscale Reynolds number. T_w and T_0 are the surface temperature on the wall and the total or stagnation gas temperature in the free stream.

The computational grid is generated by an algebraic multi-surface method (Eiseman 1985) in the (x, y)-plane which guarantees the grid orthogonality at the wall and the inflow/outflow boundaries. The grid points are clustered towards the wall and the stagnation point, but uniformly spaced in the spanwise direction. In the present LES study, a dual-grid approach is used. First, a large outer grid is generated, covering half of the ellipse downstream and extending vertically from the bottom to the top wind tunnel wall. A potential flow that matches the experimental base flow conditions is computed on this grid. For the subsequent LES calculations, a smaller inner grid covering only the leading-edge region is extracted from the outer grid. On this inner grid, the inflow/outflow boundary conditions for the mean flow can therefore be provided by the potential flow solution. This dual-grid approach enables us to improve the grid resolution near the leading edge at a reduced computational cost. For the LES grid, the minimum streamwise grid spacing is $\Delta x_{min}/D = 0.0037$ at the stagnation point, and the minimum normal spacing is $\Delta y_{min}/D = 0.00058$ at the wall. The Hiemenz scale for the laminar boundary layer, $\sqrt{\nu/A}/D = 0.0036$, is resolved by 7 grid points in the normal direction, here A is the outer flow strain rate. The time step for the present LES is $\Delta t = 0.0015$, and the total integration time $N\Delta t$ for obtaining the turbulence statistics is 25.

4.2. *Mean flow results*

The contour plots for the mean flow streamwise velocity U, transverse velocity V and temperature T are shown in figure 3. Outside the boundary layer, the difference between the mean and the laminar velocity contours are minimal, and along the stagnation streamline, the velocity profiles are almost indistinguishable (not shown here, see Xiong 2004). It confirms the experimental measurements that the stagnation-line velocity is essentially independent of the free-stream turbulence. This is, however, not the case for the temperature profile. As shown in figure 4(*a*), a steeper gradient is developed at the wall for the mean temperature profile (about 25 % higher than the laminar value), indicating the heat transfer enhancement in the presence of free-stream turbulence.

The comparisons between the mean and laminar profiles of the tangential velocity U_s and the normalized temperature $(T-1)/(T_w-1)$ are further shown in figure 4(*b–d*), using the local $s-n$ coordinates at three downstream locations $s/D = 0.2$, 0.8 and 1.6 (marked in figure 3*c*). The change of the slope at the wall is again about 25 % for the temperature and only about 5 % for the velocity, signalling a greater sensitivity to the free-stream turbulence for the heat transfer than for the skin friction. Moreover,

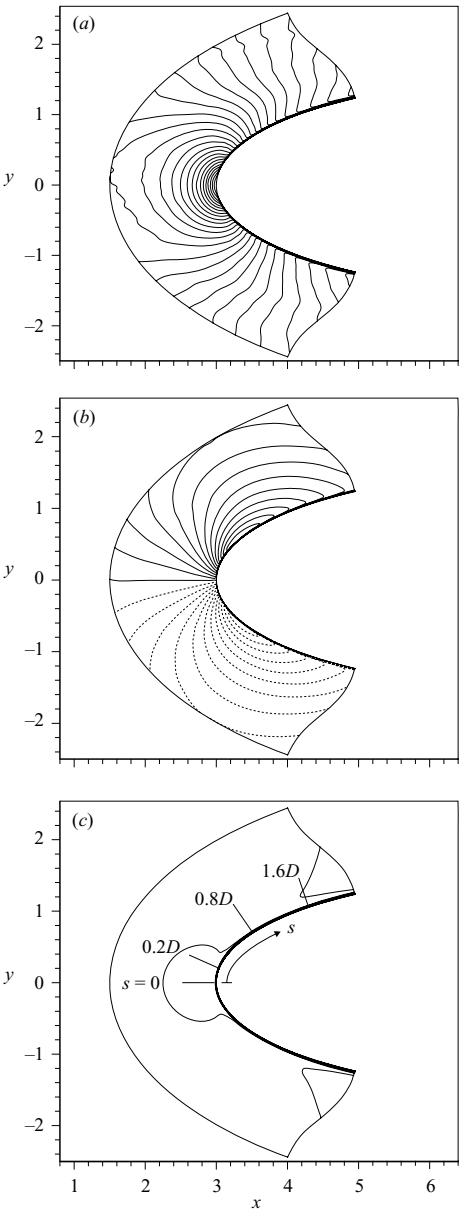

FIGURE 3. Turbulent mean velocity and temperature contours. $Re = 42\,000$, $Ma = 0.15$, $Tu = 0.05$, $L/D = 0.1$. (*a*) streamwise velocity U, contour minimum: 0, maximum: 1.3, increment: 0.05. (*b*) transverse velocity V, minimum: -0.6, maximum: 0.6, increment: 0.05. (*c*) temperature T, minimum 0.995, maximum 1.075, increment: 0.005. The streamwise locations of the four cross-sections are also marked.

the profiles of the mean streamwise velocity also show that, despite the impinging turbulence, the boundary layer remains pre-transitional. A longer streamwise distance than the present simulation domain is required before a fully turbulent boundary layer can develop.

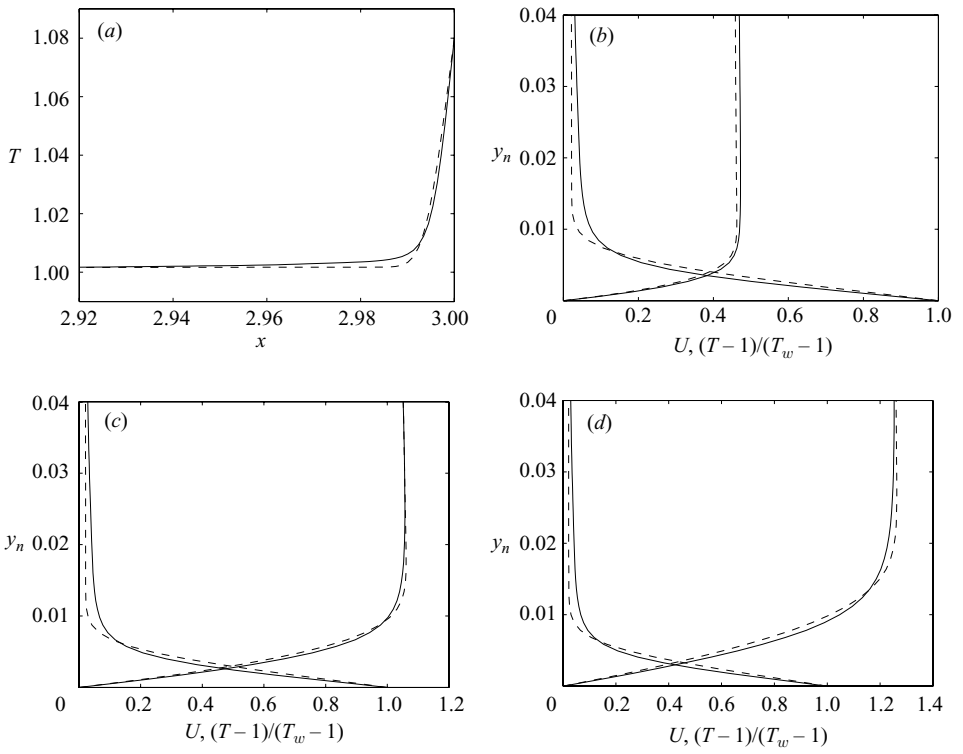

FIGURE 4. Comparison between turbulent mean and laminar velocity and temperature profiles at different streamwise locations, ——, turbulent mean; – – –, laminar. (*a*) $s/D=0$, (*b*) 0.2, (*c*) 0.8, (*d*) 1.6.

4.3. *Vortex dynamics*

Figure 5 shows a visualization of instantaneous spanwise velocity within the (x, y)-plane at $z=0$, and the temperature gradient on the model surface near the stagnation point $s=0$. It can be seen that the isotropic free-stream turbulent eddies have been strongly stretched in the streamwise direction near the stagnation point. The ensuing impingement of these vortices on the leading edge modifies the underlying thermal boundary layer dramatically. On the model surface, the resulting heat transfer distribution develops into thin, streamwise elongated streaky structures. The corresponding instantaneous temperature fields are shown in figure 6 through a series of wall normal sections at different streamwise locations. The temperature contours show distinctive mushroom-like structures. By tracing these structures in consecutive sections, we can sees the elongated streaky vortices being wrapped around the leading edge by the mean flow.

To understand better the typical vortex structures and their effects on heat transfer, the temperature contour and the corresponding velocity field in the stagnation plane $s=0$ are shown in figure 7. The velocity fields show clearly that strong, amplified y-oriented vortices produce reverse flow ($u<0$) in the stagnation region, which lifts up the hot fluid close to the wall and swaps it with the lower temperature fluid away from the wall. In doing so, the velocity disturbance creates the mushroom-like structures in the temperature contours. Directly underneath these mushroom-like structures, however, the thermal boundary layer is thicker than the undisturbed case,

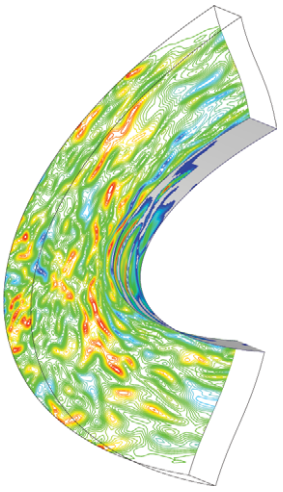

FIGURE 5. Instantaneous spanwise velocity in (x, y)-plane and temperature gradient on the body surface.

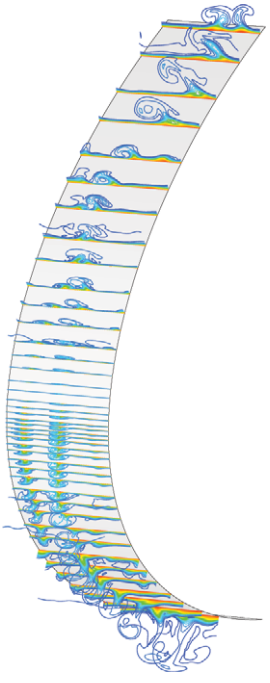

FIGURE 6. Instantaneous temperature contors at different locations on the body surface, $s/D = -0.8$ to 0.8.

and the heat transfer rate decreases. It is in the region between these mushroom-like structures, where the disturbed flow has a normal velocity directed towards the wall, that the boundary layer become thinner, and consequently the heat transfer increases. The overall spanwise averaged heat transfer rate is thus determined by the distribution and intensity of these thickened and thinned regions.

As shown in figure 7, the mushroom-like structures typically do not remain at a fixed spanwise location; instead they move laterally over a significant distance during

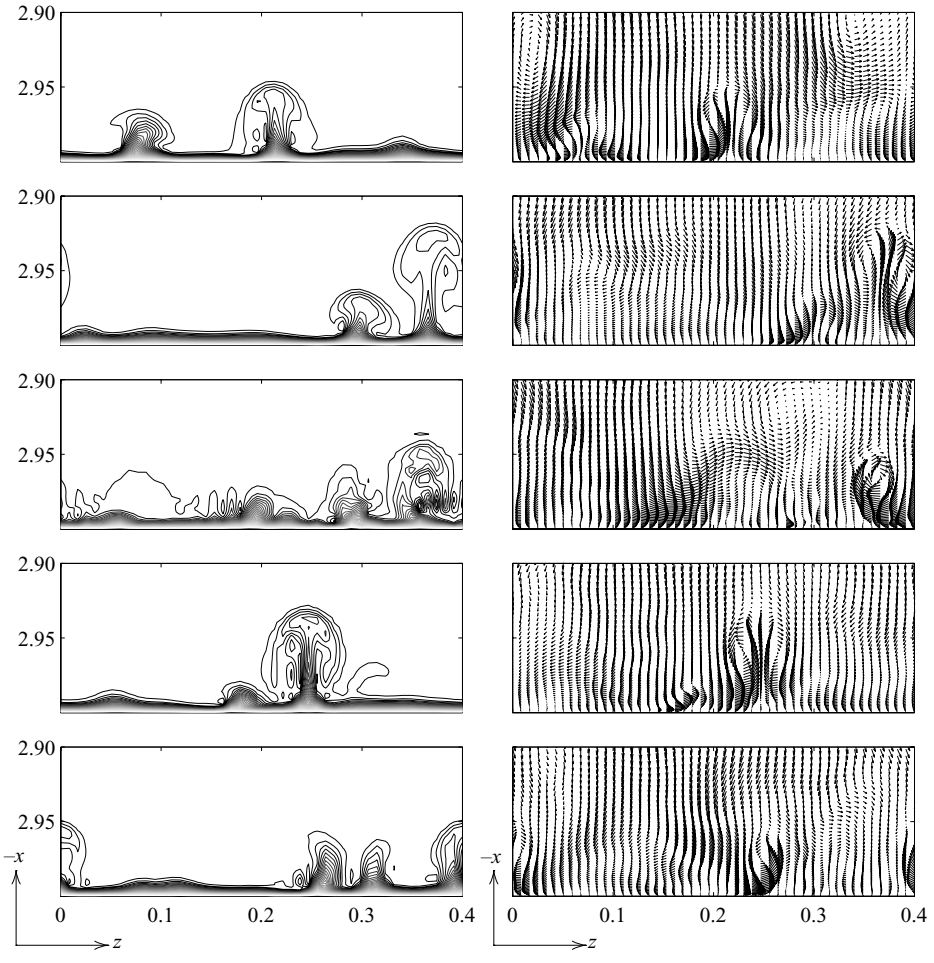

FIGURE 7. Temperature contour and the corresponding velocity field in the stagnation plane at different times. The mean flow direction is downward and the time interval is $\Delta t = 0.6$.

their lifetime. This indicates the lateral movement of the strong streamwise vortices by which these mushroom structures are formed. When a vortex approaches a wall, vorticity is generated at the wall through the no-slip boundary condition; therefore, the lateral movement of the vortices may be characterized through the movement of the wall vorticity. By following the slowest descent line on the space–time correlation, the average lateral speed for the wall vorticity along the stagnation line (z-axis) is found to be ± 0.06, which is about half of the maximum w_{rms} at the leading edge. The mechanism of the lateral movement can be understood through the so-called wall-blocking effect. Considering a single vortex approaching a wall, an inviscid image vortex with opposite sign is induced at an equal distance on the other side of the wall to enforce the no-penetration wall boundary condition. The mutual induction of these two vortices generates a tangential velocity whose magnitude is proportional to the strength of the vortices. This causes the lateral movement of the approaching vortex in the spanwise direction, and in turn the movement of the mushroom structures in the temperature contours.

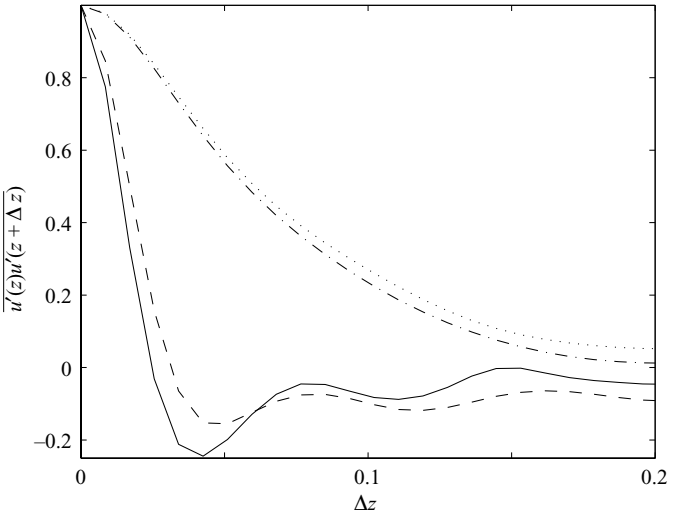

FIGURE 8. Two-point correlation of streamwise velocity in the spanwise direction along the stagnation streamline. ···, $x = 1.55D$; —·—, $x = 2.0D$; ———, $x = 2.97D$ (in the free stream); ——, $s = 2.99D$ (within the boundary layer).

The stretching of the free-stream turbulence eddies may be further characterized quantitatively using spanwise two-point correlations of velocity. Figure 8 shows the streamwise velocity correlation at different locations along the stagnation streamline. At the inflow boundary, the correlation length is long, representing the length scale of the free-stream turbulence in the absence of the strain effect. Once the turbulence enters the domain, the spanwise length scale decreases monotonically and, close to the leading edge, it reaches a scale of local boundary-layer thickness. A model problem on the competition between the amplification due to vortex stretching and damping due to viscosity in a disturbed Hiemenz boundary layer was studied by Xiong & Lele (2004), and the leading-edge region of the present flow represents the same process in the context of a complete flow field. We should also remark that because of this monotonic decrease of the turbulence spanwise length scale, the choice of the spanwise simulation domain size is a balance between encomp assing the large-scale free-stream turbulence at the inflow and sufficiently resolving the intense small-scale streamwise vortices at the leading edge. In the present LES, we place our focus at the leading-edge region and have chosen the spanwise domain size to be four times the integral length of the free-stream turbulence. A similar LES with spanwise domain size about seven times the turbulence length scale was also performed by Xiong (2004). The comparison between the two cases suggests that the LES results are not sensitive to the spanwise domain size as long as the small-scale vortices at the leading edge are adequately resolved.

The spanwise averaged non-dimensional heat transfer coefficient, denoted by Frössling number $Fr = Nu/\sqrt{Re_D}$, where Nu being the Nusselt number, is plotted in figure 9 as a function of the streamwise distance from the stagnation point. The experimental measurements from Van Fossen *et al.* (1995) are also plotted for comparison. Both the LES and experimental results show that the shape of the Fr distribution is largely the same as in the laminar case, but their values are significantly higher in the presence of free-stream turbulence. Although the present LES result is slightly lower than the experimental measurements, as not all of the

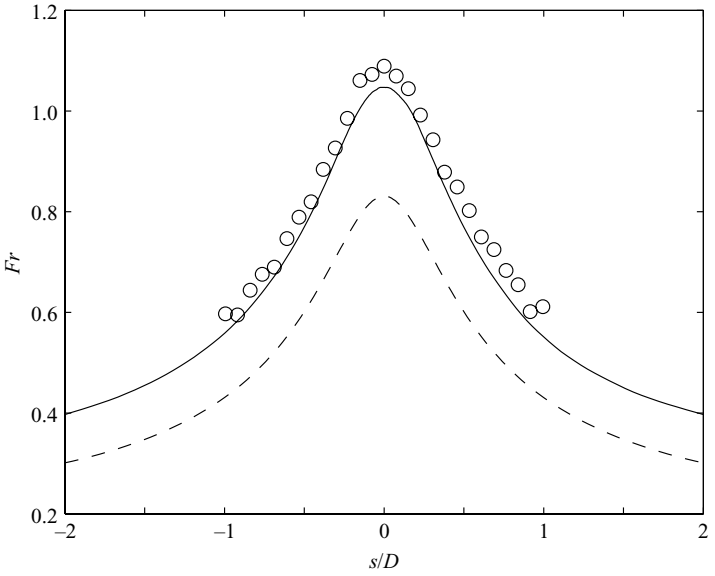

FIGURE 9. Averaged Frössling number distribution on the body surface. ——, turbulent mean; — — —, laminar; ○, experimental data (Van Fossen *et al.* 1995).

turbulence scales are resolved in LES, the overall agreement is good. As shown by Xiong & Lele (2004), there is an optimal length scale for the stagnation-point heat transfer enhancement; scales larger or smaller than the optimum produce a smaller heat transfer enhancement. In order to predict the free-stream turbulence effects accurately, it is thus important to resolve the turbulence structures up to the optimal length scale. For this reason, the effect of SGS modelling must be evaluated. A typical distribution of the instantaneous SGS eddy viscosity ν_T is shown in figure 10(a), and the corresponding time- averaged distribution is shown in figure 10(b). Both figures show that the maximum ν_T occurs in the leading-edge region, where small-scale turbulence is produced by strong vortex stretching and amplification. However, the value of ν_T is relatively small, about half of the molecular viscosity, indicating that the grid resolution close to the wall is adequate for capturing the near wall eddies. In this sense, the present LES is essentially a quasi-DNS of the near wall flow. However, because of the grid stretching in the wall normal direction, outside the boundary layer the turbulence scales are not completely captured, and we have found the SGS eddy viscosity is necessary to prevent the solution from diverging because of the intermittent passage of strongly stretched vortices outside the boundary layer.

4.4. *Reynolds stress and turbulence budgets*

Because of the spanwise homogeneity, the significant Reynolds stresses in the present flow are $\overline{u'^2}$, $\overline{v'^2}$, $\overline{w'^2}$ and $\overline{u'v'}$, and the significant heat fluxes are $\overline{u'T'}$ and $\overline{v'T'}$. Along the stagnation streamline, the symmetry in the y-direction also leads to $\overline{u'v'} = \overline{v'T'} = 0$.

It is instructive to write the governing equations for Reynolds stress and heat transport. Using the notion of the Reynolds average and letting $\overline{f}$ denote the time-laveraged value of f, we may decompose the turbulence field into a mean and a fluctuation part, i.e.

$$\rho = \overline{\rho} + \rho', \quad u_i = U_i + u_i', \quad p = P + p', \quad T = \overline{T} + T', \tag{4.1}$$

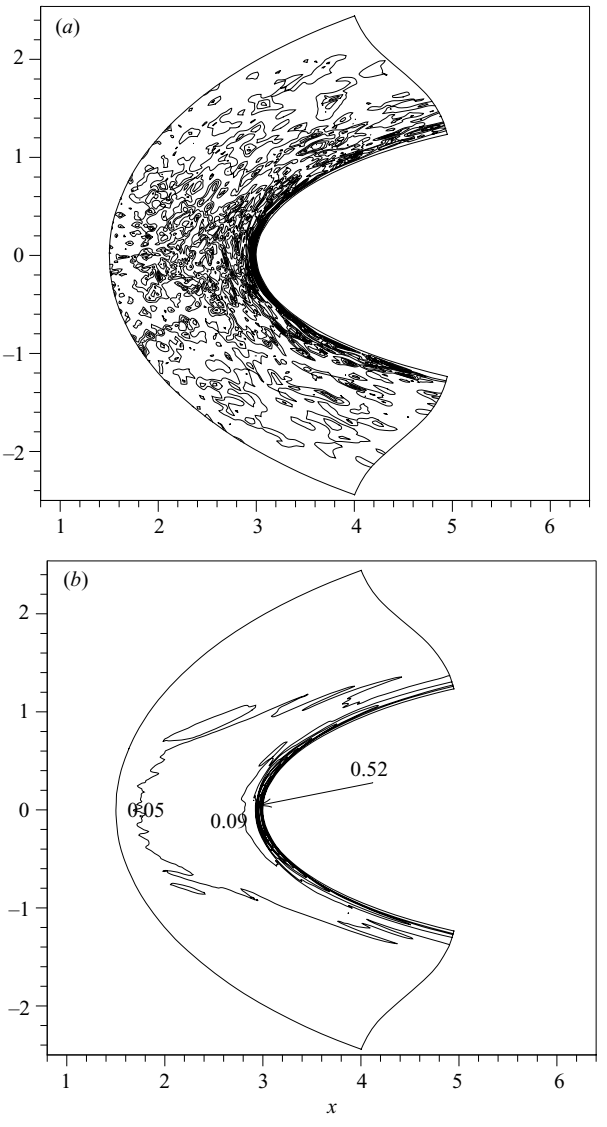

FIGURE 10. Contours of SGS eddy viscosity ν_T/ν. (*a*) Instantaneous (averaged in z), contour minimum: 0.05, maximum: 0.75, increment: 0.014. (*b*) Turbulent mean, minimum: 0.05, maximum: 0.52, increment: 0.040.

and similarly for the transport coefficients

$$\lambda = \overline{\lambda} + \lambda', \quad \mu_T = \overline{\mu} + \mu', \quad \kappa_T = \overline{\kappa} + \kappa'. \tag{4.2}$$

The steady transport equation for the Reynolds stress $\overline{u_i u_j}$ can be written as

$$\begin{aligned}\overline{\rho}\, U_k \overline{(u_i' u_j')}_{,k} = & -\overline{u_j' p_{,i}'} - \overline{u_i' p_{,j}'} - U_{i,k}[\overline{\rho}\overline{(u_k' u_j')} + U_k \overline{\rho' u_j'} + \overline{\rho' u_k' u_j'}] \\ & - U_{j,k}[\overline{\rho}\overline{(u_k' u_i')} + U_k \overline{\rho' u_i'} + \overline{\rho' u_k' u_i'}] - \overline{\rho}\, \overline{u_k'(u_i' u_j')_{,k}} - \overline{\rho' u_k'(u_i' u_j')_{,k}} + \Phi_T.\end{aligned} \tag{4.3}$$

On the right-hand side of (4.3), the first two terms are the velocity pressure gradient correlation; the third and fourth terms are the production terms; the fifth and

sixth terms are the transport of Reynolds stress due to turbulent fluctuation. For incompressible flow, it can be reduced to a divergence form and is termed as turbulence transport. Here, for compressible flow, we use the term turbulence convection to refer to the sum of these two terms. The Φ_T in the last row is the total dissipation

$$\begin{aligned}\Phi_T = &\frac{1}{Re}\left[(\overline{\lambda}\,\overline{D'_{,i}u'_j} + \overline{D}_{,i}\,\overline{\lambda' u'_j} + \overline{\lambda' D'_{,i}u'_j}) + (\overline{\lambda}\,\overline{D'_{,j}u'_i} + \overline{D}_{,j}\,\overline{\lambda' u'_i} + \overline{\lambda' D'_{,j}u'_i})\right] \\ &+ \frac{2}{Re}\left[(\overline{\mu}\overline{S'_{ik,k}u'_j} + \overline{S}_{ik,k}\,\overline{\mu' u'_j} + \overline{\mu' S'_{ik,k}u'_j}) + (\overline{\mu}\overline{S'_{jk,k}u'_i} + \overline{S}_{jk,k}\,\overline{\mu' u'_i} + \overline{\mu' S'_{jk,k}u'_i})\right] \\ &= \varepsilon + \Phi_v, \end{aligned} \tag{4.4}$$

where $D \equiv u_{i,i}$ is the divergence of the velocity field; ε is the turbulence dissipation rate defined by

$$\varepsilon = \frac{2}{Re}\,\overline{\mu}\,\overline{u'_{i,k}\,u'_{j,k}}, \tag{4.5}$$

and the remaining term $\Phi_v = \Phi_T - \varepsilon$ is loosely termed viscous diffusion by analogy to the incompressible flow case, although it also contains terms involving dilatation and fluctuation in the turbulent viscosity coefficient.

Similarly, for turbulence heat flux $\overline{u'_i T'}$, we may also write

$$\begin{aligned}\overline{\rho} U_k \overline{(u'_i T')_{,k}} = &- \overline{T' p'_{,i}} - \overline{T}_{,k}[\overline{\rho}\overline{u'_k u'_i} + U_k \overline{\rho' u'_i} + \overline{\rho' u'_k u'_i}] \\ &- U_{i,k}[\overline{\rho}\overline{u'_k T'} + U_k \overline{\rho' T'} + \overline{\rho' u'_k T'}] - \overline{\rho}\,\overline{u'_k (u'_i T')_{,k}} - U_k \overline{\rho' (u'_i T')_{,k}} - \overline{\rho' u'_k (u'_i T')_{,k}} \\ &+ \frac{\gamma}{Pr\,Re}[\overline{\kappa} \overline{u'_i T'_{,kk}} + \overline{\kappa' u'_i}\,\overline{T}_{,kk} + \overline{\kappa' u'_i T'_{,kk}}] + \Phi_p + \Phi_H. \end{aligned} \tag{4.6}$$

On the right-hand side of (4.6), the first term is the temperature pressure gradient correlation; the second and the third terms are the heat flux production; the fourth to sixth terms are the turbulence convection and the seventh term is the turbulent heat conduction. The last two terms, Φ_p and Φ_H are the pressure dilatation work and viscous dissipation. The expressions for Φ_p and Φ_H are omitted here; they are not important in the present flow.

4.5. *Turbulence intensity along the stagnation streamline*

The change of the different components of turbulence intensity characterizes the anisotropy of stagnating turbulence. The root-mean-square value of velocity fluctuation along the stagnation streamline is shown in figure 11. The combination of the turbulence length scale and the close location of the inflow boundary largely eliminates the free decaying stage of the free-stream turbulence. After a relatively balanced, isotropic development before $x \sim 2.4$, the turbulence develops strong anisotropy between $x \sim 2.4$ and 2.7. Within this region, both u_{rms} and w_{rms} increase but v_{rms} decreases, which is consistent with the prediction of RDT (Hunt 1973), indicating that the dominant mechanism for the turbulence anisotropy is by vortex stretching (Lee & Reynolds 1985) in the y-direction. At closer distances $x > 2.7$, the presence of the model surface generates a pronounced inviscid blocking effect. By the non-penetration boundary condition, the normal velocity, u_{rms}, must vanish at the wall. This causes u_{rms} to decay over a distance of the order of the turbulence integral length scale, typically larger than the boundary-layer thickness. As a result, the kinetic energy of u_{rms} is partially redistributed into v and w components, leading not only to a further increase in w_{rms}, but also to an increase in v_{rms} that was previously decreasing. Very near to the wall, the viscous effect dominates and all the turbulence vanishes on the wall. The evolution of the turbulence anisotropy may

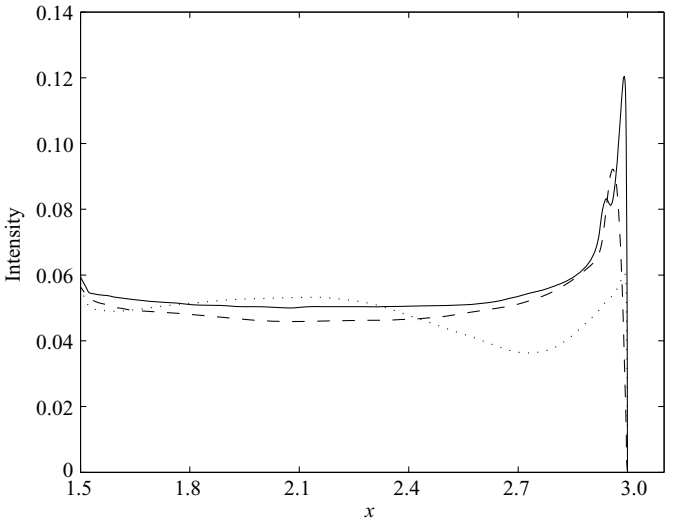

FIGURE 11. Turbulence intensity along the stagnation streamline. ———, u_{rms}; · · ·, v_{rms}; ——, w_{rms}.

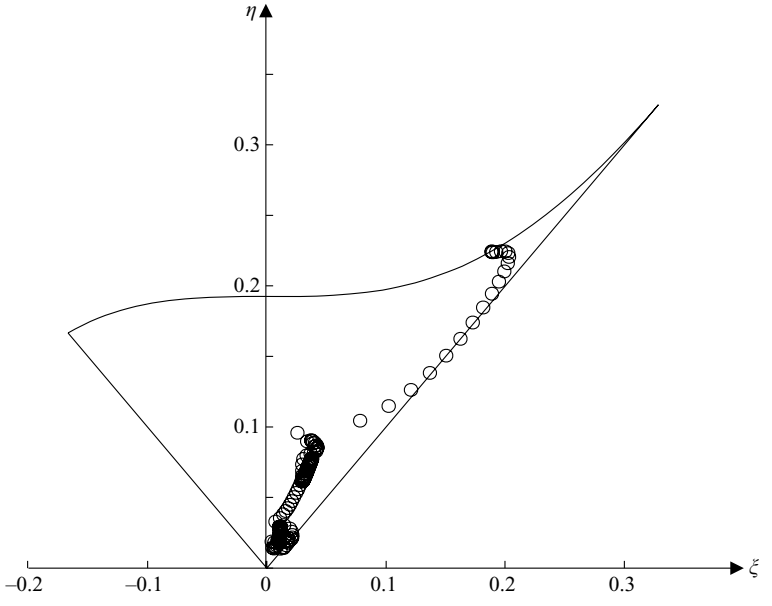

FIGURE 12. The evolution of the Reynolds-stress invariants along the stagnation streamline.

also be characterized by the trajectory in the plane of the invariants ξ and η, here $\xi = (III_b/2)^{1/3}$, $\eta = (-II_b/3)^{1/2}$, and II_b and III_b are the second and third invariants of the Reynolds stress anisotropy tensor $b_{ij} = \overline{u_i u_j}/\overline{u_k u_k} - \delta_{ij}/3$ (Pope 2000). This is shown in figure 12 by the discrete dots representing different locations along the stagnation streamline. It can be seen that from a nearly isotropic state, the Reynolds stress anisotropy develops as the stagnation point is approached and reaches a peak value $\eta = 0.225$ inside the boundary layer. The turning point around $\eta = 0.1$ corresponds to the peak location of u_{rms} in figure 11, demarcating the beginning of significant inviscid blocking effect.

4.6. *Turbulence budgets along the stagnation streamline*

The budgets for the normal Reynolds stresses, $\overline{u'^2}$, $\overline{v'^2}$ and $\overline{w'^2}$, along the stagnation streamline are shown in figure 13. In these figures, the total dissipation Φ_T is used as the dissipation term. For $\overline{u'^2}$, the production term $-\overline{u'^2}\partial U/\partial x$ is associated with the mean flow strain rate, representing an energy transfer from the mean flow to $\overline{u'^2}$. Conversely, the production for $\overline{v'^2}$ is $-\overline{v'^2}\partial V/\partial y$, which has an opposite sign and represents an energy transfer back to the mean flow. There is no production term for $\overline{w'^2}$ because the mean flow is two-dimensional. The turbulence transport has the largest magnitude in $\overline{u'^2}$, but is confined mostly to the near-wall region. It changes sign as the wall is approached, and if integrated along the stagnation line, it results in a vanishing net contribution to the turbulence energy. Turbulent convection is not important for $\overline{v'^2}$ as compared to other terms. For $\overline{w'^2}$, we found that the turbulent convection term largely cancels the mean convection term, and the sum of these two exerts a weak dissipative effect on $\overline{w'^2}$. The total dissipation extends farthest from the wall for $\overline{u'^2}$ and closest for $\overline{v'^2}$. It has the largest value for $\overline{w'^2}$, yet the smallest for $\overline{u'^2}$. Except for $\overline{w'^2}$, the dissipation term does not play a significant role along the stagnation line except extremely close to the wall for $\overline{v'^2}$.

Of particular interest for the stagnating turbulence is the redistribution term, i.e. the correlation between velocity and pressure gradient. Along the stagnation streamline, it is comparable in magnitude for all three normal Reynolds stresses. In strain-dominated flows, its primary effect is the generation of turbulence anisotropy. Being largely negative in figure 13(a) for $\overline{u'^2}$, it is positive for $\overline{v'^2}$ and $\overline{w'^2}$, as shown in figures 13(b) and 13(c). Hence, It represents a redistribution of the energy from $\overline{u'^2}$ to $\overline{v'^2}$ and $\overline{w'^2}$. In fact, for $\overline{v'^2}$ and $\overline{w'^2}$, it is the only major energy input. For $\overline{v'^2}$, it balances with the negative production term, whereas for $\overline{w'^2}$, the balance is with viscous dissipation and the total convection.

It is instructive to compare the energy redistribution obtained by the present LES and those by Reynolds averaged Navier–Stokes (RANS) simulations. In the RANS simulations of Im *et al.* (2002), three Reynolds stress models (GL, GL-CL and SSG models) along with the conventional $k-\epsilon$ model, are used to compute impinging and countercurrent jets. It is shown that in the strain-dominated flows, the overall predicative capability of the Reynolds stress models depends crucially on the correct modelling of the pressure- strain correlation, which is part of the redistributive velocity pressure-gradient term. Thus in § 5, we will examine the eddy viscosity and the pressure-strain correlation from the present LES and compare them with the corresponding Reynolds stress models.

4.7. *Fluctuations in local $s-n$ coordinates*

Using the local s–n coordinates, the profiles of $\overline{u_s'^2}$, $\overline{u_n'^2}$ and $\overline{w'^2}$ at $s/D=0,\ 0.2,\ 0.8,\ 1.6$ are plotted in figure 14. The local boundary-layer thickness at the corresponding locations are also marked on the right-hand side. Note that because of the symmetry at the stagnation streamline, the profile of $\overline{u'^2}$ is actually shown in figure 14(a) as $\overline{u_n'^2}$ (at $s=0$), whereas the $\overline{u_s'^2}$ at $s=0$ in figure 14(a) is actually $\overline{v'^2}$. This correspondence holds only along the stagnation streamline.

Near stagnation point $s=0$, the magnitude of streamwise fluctuation is small because it corresponds to the velocity fluctuation in the axial direction of the strongly stretched vortices. At locations $s>0$, however, the streamwise vortices become embedded in the mean boundary-layer shear flow, and are therefore capable of generating large streamwise momentum exchange in the wall normal direction. This is demonstrated by the increase of the magnitude of $\overline{u_s'^2}$ on moving downstream. Also

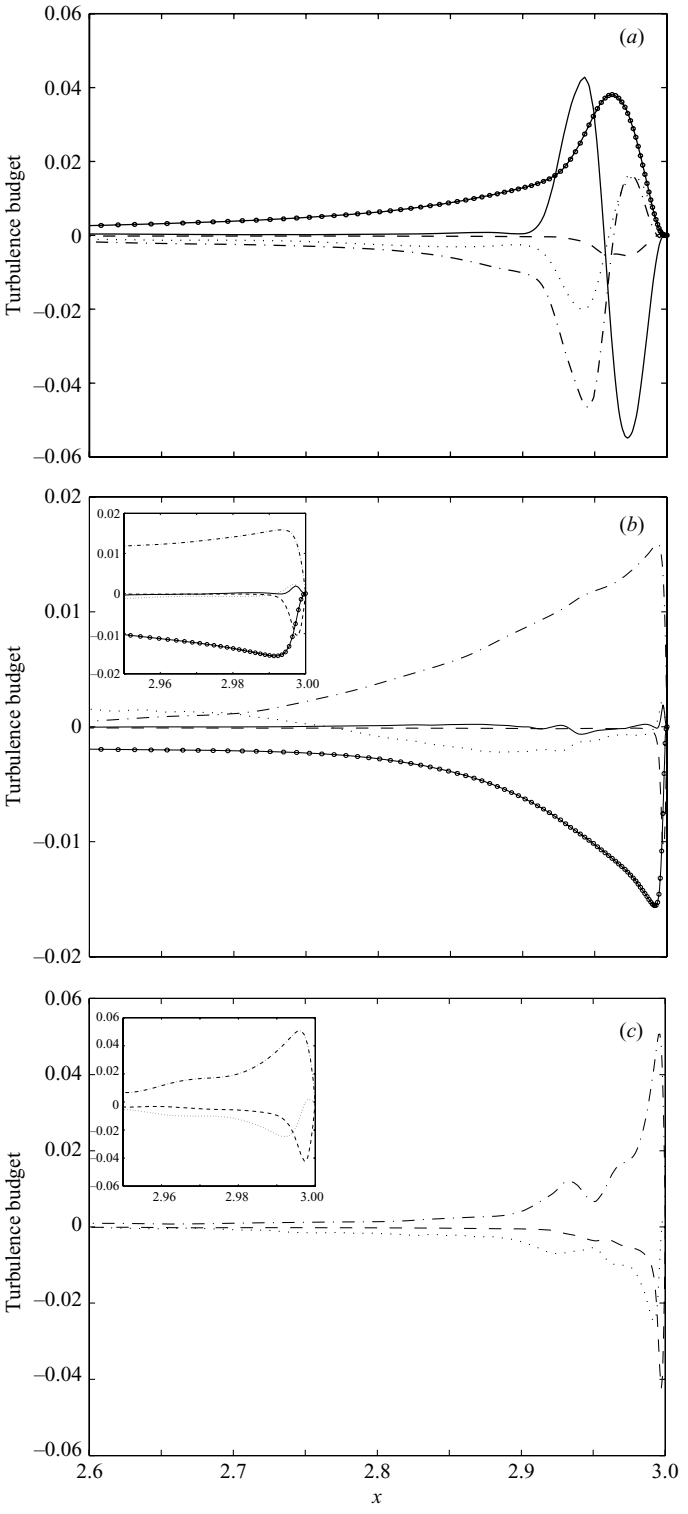

FIGURE 13. Turbulence budget along the stagnation streamline. (*a*) $\overline{u'^2}$, (*b*) $\overline{v'^2}$, (*c*) $\overline{w'^2}$, —∘—, production; ———, dissipation; ···, mean convection (*a*) and (*b*), mean convection + turbulent convection (*c*); ——, turbulent convection; —·—, velocity pressure gradient correlation.

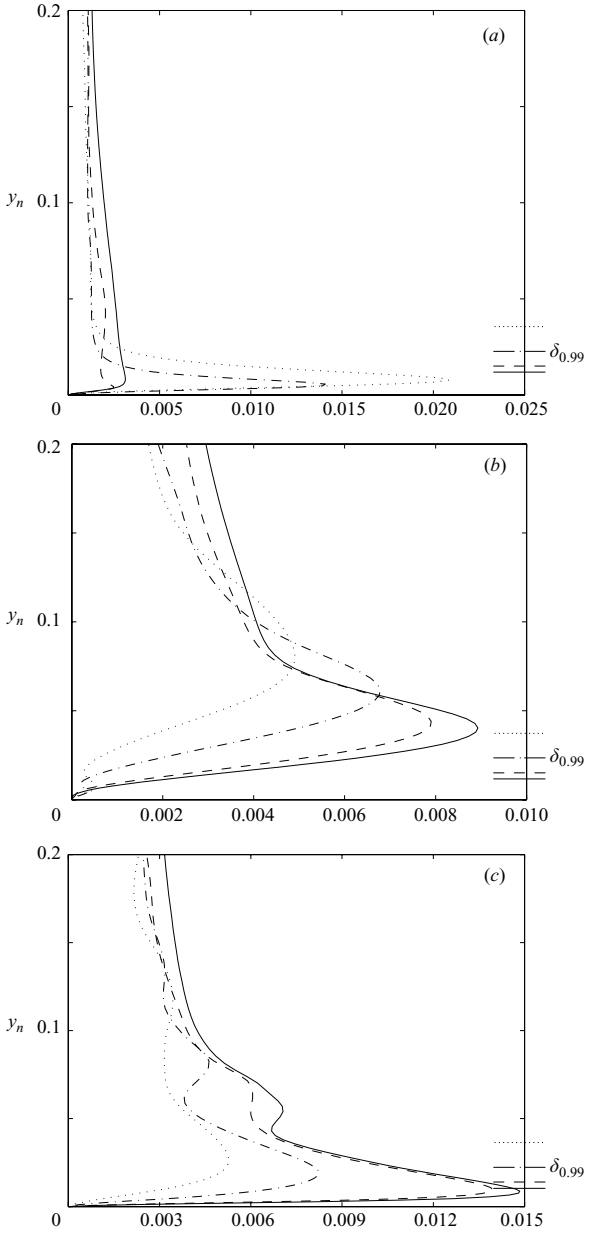

FIGURE 14. The profiles of tangential, normal and spanwise velocity fluctuation at different streamwise locations. The corresponding laminar boundary-layer thickness $\delta_{0.99}$ is marked on the right-hand side. ——, $s=0$; – – –, $s=0.2D$; — · —, $s=0.8D$; · · ·, $s=1.6D$. $(s-n)$ coordinates. (*a*) $\overline{u_s'^2}$, (*b*) $\overline{u_n'^2}$, (*c*) $\overline{w'^2}$.

notice that the peak of $\overline{u_s'^2}$ measured in local boundary-layer thickness is becoming closer to the wall downstream, showing the characteristics of a transitional boundary-layer.

The term $\overline{u_n'^2}$ shows its highest peak value at $s=0$ where the vortex stretching is strongest, and then decreases downstream. It becomes significantly smaller than the

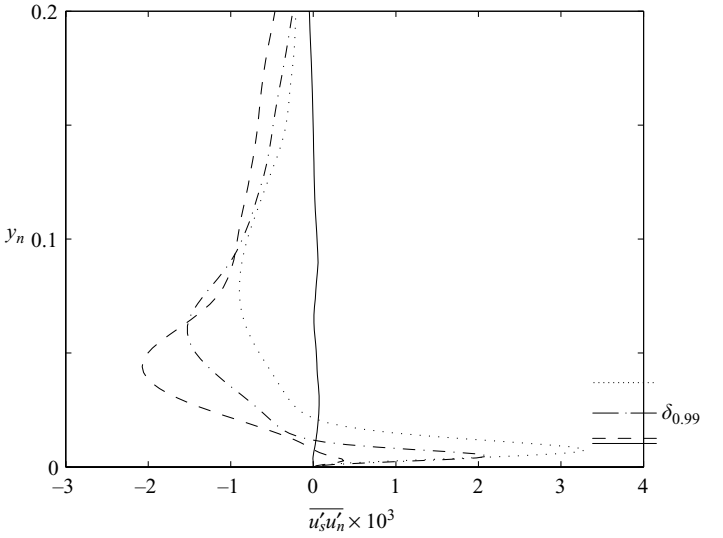

FIGURE 15. The profiles of turbulent Reynolds stress $\overline{u'_s u'_n}$ at different streamwise locations. The corresponding laminar boundary-layer thickness $\delta_{0.99}$ is marked on the right-hand side. ——, $s = 0$; – – –, $s = 0.2D$; — · —, $s = 0.8D$; · · ·, $s = 1.6D$. (s–n) coordinates.

streamwise fluctuation $\overline{u'^2_s}$ at the downstream locations, indicating that the turbulence there is mainly dominated by strong shear. Moreover, figure 14(*b*) also demonstrates the wall-blocking effect extending to a distance of the order of the turbulence integral scale, which explains the peaks of $\overline{u'^2_n}$ outside the boundary layer.

For the spanwise fluctuation $\overline{w'^2}$, figure 14(*c*) shows that its amplitude also decays monotonically downstream from the stagnation point. As mentioned before, the strong mean flow-straining and wall-blocking effects decrease on moving downstream, and the flow gradually changes to a shear-dominated type. In such cases, the redistribution term plays a much smaller role in transferring the turbulence kinetic energy from $\overline{u'^2}$ to $\overline{w'^2}$, yet there is no production term for $\overline{w'^2}$. The combination of these factors determines the trend of the decreasing $\overline{w'^2}$ in the streamwise direction. Another feature of the $\overline{w'^2}$ profile is that besides the main peak inside the boundary layer, a second peak develops outside the boundary layer in the leading-edge region ($s/D < 0.8$). We believe that this is yet another indication of the turbulence anisotropy resulting from the existence of the strong streamwise vortices. Far from the leading edge, the free-stream turbulence is isotropic, and the turbulence vortices are orientated randomly with no preferred direction. As it approaches the stagnation point, turbulence anisotropy develops because of the strong streamwise vortices emerging from the background turbulence. If these vortices were perfectly stationary then they would appear in the mean flow, but they are induced by free-stream turbulence and thus form and decay and move about as well. One of the characteristics of the streamwise vortices is that the spanwise velocity w changes sign across the vortex section, and thus its room-mean-square value has a two-peak structure with the lowest point in between corresponding to the vortex centre. The two peaks are not of equal strength, since the magnitude of w' is increasing. When these streamwise vortices become strong and frequent enough, this particular pattern, super-imposed on the background turbulence field, gives rise to the second peak in the overall w'_{rms}.

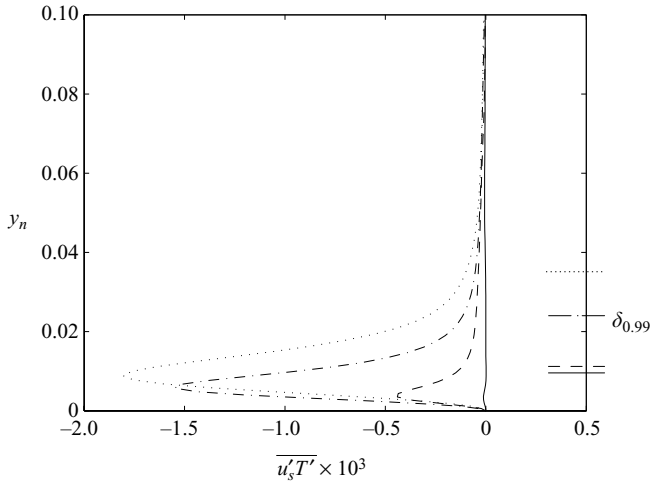

FIGURE 16. The profiles of tangential heat flux $\overline{u_s'T'}$ at different streamwise locations. The corresponding laminar boundary-layer thickness $\delta_{0.99}$ is marked on the right-hand side. ——, $s=0$; – – –, $s=0.2D$; — · —, $s=0.8D$; · · ·, $s=1.6D$. (s–n) coordinates.

The only significant shear stress in the present flow is $\overline{u'v'}$ and it vanishes on the stagnation streamline due to the symmetry in velocity u and v. In figure 15, the profiles of $\overline{u_s'u_n'}$ are plotted in local $s-n$ coordinates. There are two distinct peaks for each curve, one being negative outside the boundary layer, and the other positive inside the boundary layer. Moving downstream from the stagnation point, we find the amplitude of the outer peak decreases whereas the amplitude of the inner peak increases. The inner positive peak of $\overline{u_s'u_n'}$ represents a counter-gradient hence non-local transport of momentum, and this is believed to be a result of the vortex rebounding at the wall. Essentially, mean convection brings the stretched turbulence eddies from the free stream into the laminar boundary layer and aligns the vortices in the streamwise direction. As these streamwise vortices approach the wall, the no-slip wall boundary condition enforces two thin regions of large vorticity (with opposite sign to the approaching vortices) to be generated between the wall and the approaching vortices. When the streamwise vortices are strong enough, the thin underneath region can be lifted up and it forms a dipole vortex with the primary vortex. This newly formed dipole vortex induces a positive normal velocity and the vortex bounces back from the wall. The mechanism of rebounding vortex has been previously studied in detail using a pair of counter-rotating vortices, or a dipole vortex, colliding with a wall under self-induced velocity (Orlandi 1990; Carnevale, Velasco Fuentes & Orlandi 1997). Here in the leading-edge region, the vortices are convected by the mean flow (thus a vortex pair is not required), but the vortex–wall interaction is similar. In terms of fluctuation velocity, when turbulence is brought into the boundary layer from the free stream, it creates a region of $u_s'>0$, $u_n'<0$ within the boundary layer which is responsible for the overall negative $\overline{u_s'u_n'}$. However, because of the vortex rebounding, the normal velocity u_n' changes sign in the near-wall region and consequently generates the positive value of $\overline{u_s'u_n'}$.

4.8. *Thermal fluxes* $\overline{u_s'T'}$ *and* $\overline{u_n'T'}$

The profiles of the thermal fluxes $\overline{u_s'T'}$ and $\overline{u_n'T'}$ are shown in figures 16 and 17 at different streamwise locations. While the tangential flux $\overline{u_s'T'}$ increases on moving

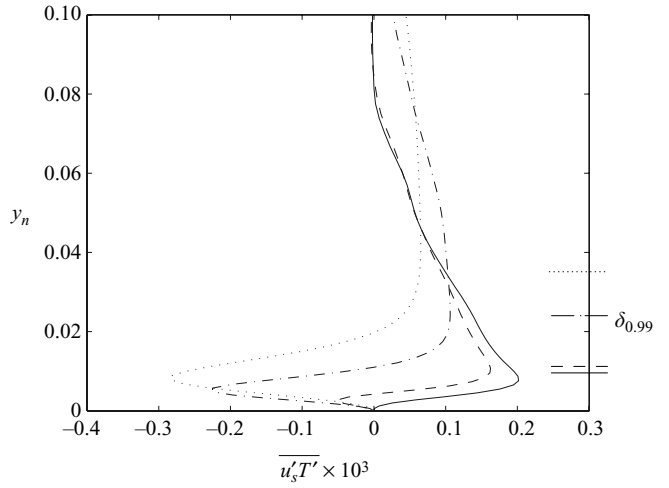

FIGURE 17. The profiles of wall normal heat flux $\overline{u_n'T'}$ at different streamwise locations. The corresponding laminar boundary-layer thickness $\delta_{0.99}$ is marked on the right-hand side. ——, $s=0$; – – –; $s=0.2D$; — · —, $s=0.8D$; · · ·, $s=1.6D$. (s–n) coordinates.

downstream, the peak value of the positive normal flux $\overline{u_n'T'}$ decreases. Near the stagnation point, the $\overline{u_n'T'}$ is predominantly positive owing to the same free-stream turbulence impingement that gives rise to the negative shear stress $\overline{u_s'u_n'}$. Different from that of the $\overline{u_s'u_n'}$, however, is the peak location of the $\overline{u_n'T'}$. Comparing figures 17 and 15, one can see the positive peak of $\overline{u_n'T'}$ is almost five times closer to the wall than the negative peak of $\overline{u_s'u_n'}$. We believe this difference in the peak locations between the thermal flux and the shear stress explains the greater sensitivity to the free-stream turbulence for the heat transfer rate than the wall friction coefficient, as observed in figure 4. Close to the wall at downstream locations, $\overline{u_n'T'}$ changes sign, indicating the similar counter-gradient feature in the thermal fluxes. The mechanism can be understood in a similar way through the vortex rebound as for $\overline{u_s'u_n'}$ discussed in § 4.7. The profiles of the production terms for $\overline{u'T'}$ and $\overline{v'T'}$ are shown in figures 18 and 19. Along the streamwise direction, the $\overline{u'T'}$ increases but $\overline{v'T'}$ decreases. The decaying of the production in $\overline{v'T'}$ may be attributed to the difference in the peak locations of the fluctuation velocity v' and temperature T'. The former shifts away from the wall downstream whereas the latter remains close to the wall in the entire streamwise range.

5. Eddy viscosity and pressure–strain correlation

As mentioned in § 1, modelling turbulence effects in strain dominated flows remains a challenge. One of the primary goals of the present LES study is to provide useful information for this effort. Conventional two-equation models do not address the anisotropy of stagnating turbulence, and the use of the linear constitutive model, $\overline{u_i'u_j'} = -2\nu_T S_{ij} + 2/3k\delta_{ij}$, results in severe overprediction of the turbulence production. In order to recover the correct turbulence production, one remedy (Durbin 1996) based on the realizability consideration introduces an upper bound on the eddy viscosity, $\nu_T \leqslant k/\sqrt{6}|S|$, where $|S|$ is the magnitude of the strain rate. In practice, the constraint can also be expressed in terms of turbulence time scale T by using formula $\nu_T = C_\mu kT$. For example, $T = \min\{k/\epsilon, \alpha/\sqrt{6}C_\mu|S|\}$, where $\alpha = 0.6$, has been incorporated into

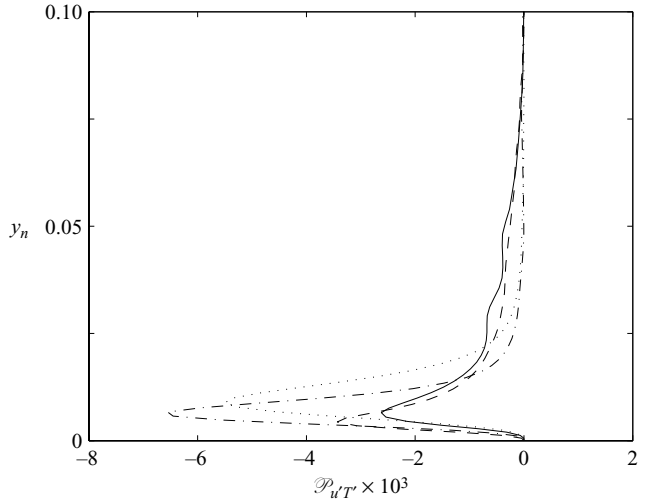

FIGURE 18. Profiles of turbulence production for $\overline{u'T'}$ along the wall normal direction. ——, $s = 0$; – – –, $s = 0.2D$; — · —, $s = 0.8D$; and · · ·, $s = 1.6D$.

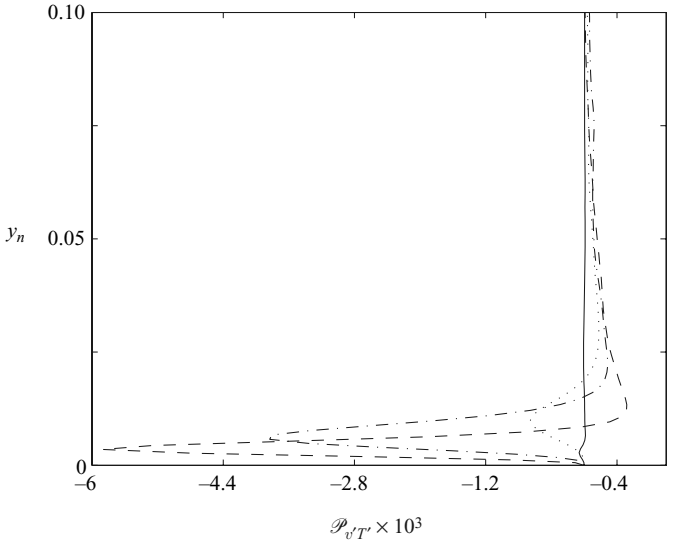

FIGURE 19. Profiles of turbulence production for $\overline{v'T'}$ along wall normal direction. ——, $s = 0$; – – –, $s = 0.2D$; — · —, $s = 0.8D$; · · ·, $s = 1.6D$.

the standard $k - \epsilon$ model to compute turbine blade heat transfer (Medic & Durbin 2002). For the realizability condition, figure 20 shows the normalized turbulence eddy viscosity ν_T (not the SGS eddy viscosity) and the corresponding $\nu_{TR} = k/\sqrt{6}|S|$ along the stagnation line based on the present LES results. The effective ν_T is obtained through $\mathscr{P} = 2\nu_T S_{ij} S_{ij}$ with the turbulence production $\mathscr{P}$ and strain rate S_{ij} computed from the LES results. As a comparison, the eddy viscosity obtained using the conventional $k - \epsilon$ model $\nu_{Tk} = C_\mu k^2/\epsilon$, $C_\mu = 0.09$ is also plotted. Away from the stagnation point, the value of ν_{Tk} is about five times that of ν_T. Close to the stagnation point, ν_{Tk} decreases and approaches a constant value of about twice ν_T. Because of

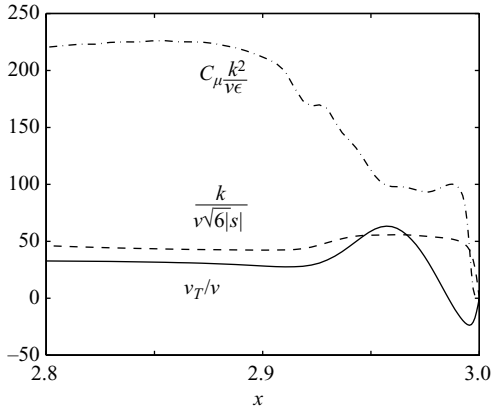

FIGURE 20. Turbulence eddy viscosity ν_T (not the SGS ν_T). ——, LES results; —·—, $k-\epsilon$ model; – – –, realizability constraint.

this elevated eddy vicosity, the $k-\epsilon$ model overpredicts the turbulence production in stagnation-point flows. On the other hand, the eddy viscosity ν_{TR} tracks the ν_T quite well and provides a useful upper bound for ν_T, indicating the effectiveness of the realizability constraints.

In second-order Reynolds stress models, the pressure–strain correlation

$$\phi_{ij} = \overline{\frac{p'}{\rho}\left(\frac{\partial u_i}{\partial x_j} + \frac{\partial u_j}{\partial x_i}\right)}, \tag{5.1}$$

is the primary means of redistributing the kinetic energy among different components of the Reynolds stresses. The current LES results can be used to examine the particular pressure–strain correlations in different Reynolds stress models. Here three of such turbulence models are chosen that were used in Im *et al.* (2002): the GL (with wall reflection terms); GL-CL; and SSG models. Figure 21 shows the comparison of the $\phi_{\alpha\alpha}$ along the stagnation streamline between the LES results and the turbulence models (see Appendix B for the expressions of $\phi_{\alpha\alpha}$ in these models). First, notice that in the region close to the stagnation point, the GL model predicts all three components of $\phi_{\alpha\alpha}$ with the wrong sign. Between the GL-CL and the SSG models, the GL-CL is significantly better at predicting ϕ_{11} and ϕ_{33}; not only is the sign more consistent, the magnitudes are also comparable to the LES results. The LES data show the ϕ_{22} is smaller than the other two components, this is, however, not apparent in the model predictions. Both GL-CL and SSG models severely overpredict ϕ_{22} with the GL-CL model having the largest error, albeit a more consistent sign. Another feature of the GL-CL model is that the peaks of the $\phi_{\alpha\alpha}$ are located at a larger distance from the wall than the LES results. These findings are consistent with the observations made by Im *et al.* (2002) from the RANS calculations and suggest that the GL-CL model is overall the most effective of the three turbulence models for stagnation-point or strain-dominated flows.

6. Concluding remarks

In this paper, the stagnation-point flow and heat transfer at an elliptical isothermal leading edge in the presence of free-stream turbulence is investigated using LES. Along the stagnation streamline, the turbulence intensity in the streamwise (x) and

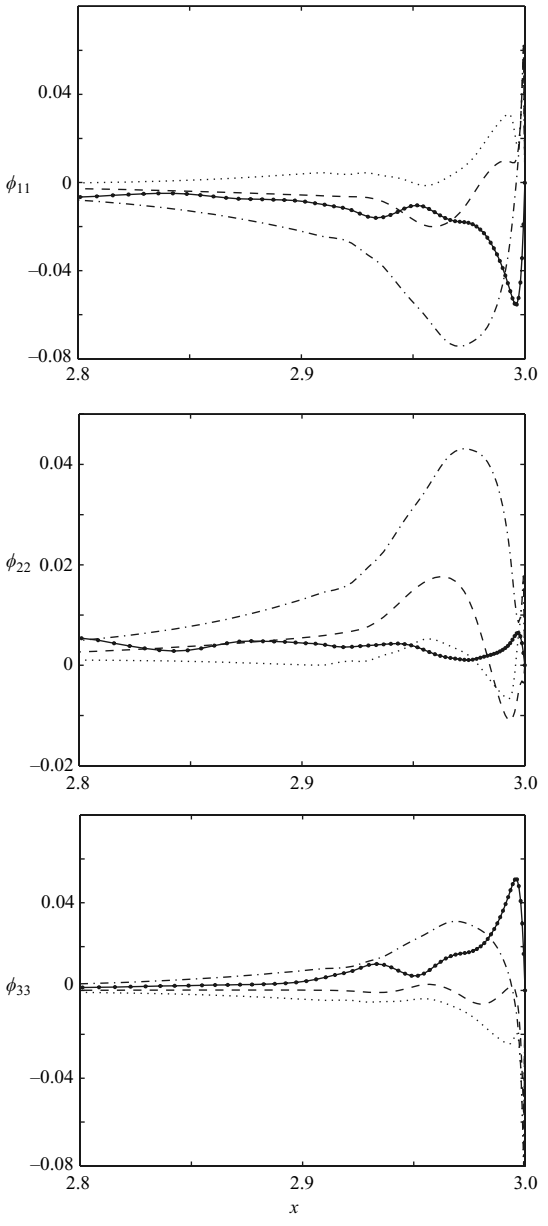

FIGURE 21. The pressure–strain correlation $\phi_{\alpha\alpha} = \overline{(p'/\rho)(\partial u_\alpha/\partial x_\alpha)}$ (no summation over α) along the stagnation streamline, comparison between the LES results and different Reynolds stress models. —○—, LES; ···, GL model; —•—, GL-CL model; —, SSG model.

spanwise (z) directions increases, whereas the intensity in the transverse (y) direction decreases. Very close to the wall, the streamwise fluctuation is reduced by the wall blockage effect, and its energy is transferred to the other two components. As a result, the spanwise turbulence intensity becomes the most dominant of the three components in this region. The most important Reynolds stress budget terms for the stagnating turbulence are the production and the velocity pressure gradient correlation. In particular, the latter dominates the development of the transverse

and spanwise normal Reynolds stresses, and hence the turbulence anisotropy. The boundary layer under free-stream turbulence is found to be in non-equilibrium and pre-transitional. The normal turbulence heat flux is shown to have a peak location much closer to the wall than that for the Reynolds shear stress, explaining the greater sensitivity to free-stream turbulence for the heat transfer than the momentum transfer in stagnation-point flows.

Intense, streamwise vortical structures generated at the leading edge owing to strong vortex stretching are found to be the direct cause of the heat transfer enhancement. These vortices have a spanwise dimension about 2–3 times the local boundary-layer thickness and they move laterally at a speed comparable to the local spanwise fluctuation velocity. The enhancement of the heat transfer obtained by the present LES agrees well with the corresponding experimental measurements.

The LES results are used to examine the eddy viscosity obtained from the conventional $k-\epsilon$ model and from realizability conditions. The $k-\epsilon$ model is found to produce excessive turbulent eddy viscosity in stagnation-point flows, but the realizability condition provides an adequate upper bound for the eddy viscosity. Furthermore, the pressure–strain correlations obtained by the present LES are compared with those from three Reynolds stress models (GL, GL-CL and SSG). Of the three models, it is found that the GL-CL model provides the most effective pressure–strain correlations in stagnation-point or strain-dominated flows. It is hoped that the LES data will be useful in developing improved models of pressure–strain correlations for strain-dominated flows.

This work was supported by the Air Force Office of Scientific Research under grant F49620-01-1-0138 with Dr Tom Beutner as the programme manager. The computer resource was provided by DoD Major Shared Resource Center at US Army Engineer Research and Development Center, and Army Research Laboratory. We appreciate the referees' comments on the original manuscript, particularly those concerning the Reynolds stress models.

Appendix A. Validation

Laminar compressible boundary-layer profiles at the leading edge allow self-similar analytic solutions when viscosity varies as a linear function of temperature (Reshotko & Beckwith 1957). Figures 22 and 23 show the velocity and enthalpy profiles for $Pr=1$ for flow over an elliptical leading edge. The wall temperature is set to be twice the total temperature of the incoming flow, i.e. $T_w/T_0=2$. For different Mach numbers, $Ma=0.1$ and $Ma=0.8$ (not shown here), excellent agreement in the velocity and enthalpy profiles is obtained between the numerical and analytical solution. Further comparisons at different flow conditions can be found in Xiong (2004). To validate the code in unsteady computations, we choose to compute the boundary-layer receptivity to ambient sound at a blunt leading edge. Receptivity is defined as a process by which external flow disturbances are converted into instability waves (Morkovin 1969). For the flat-plate boundary-layer flow, the sound receptivity refers to the generation of Tollmien–Schlichting (T-S) instability waves inside the boundary layer by free-stream acoustic waves. We use the same flow configuration as in Lin (1992) and Collis (1997) for a compressible boundary layer on a flat plate with a super ellipse leading edge. However, unlike the usual numerical receptivity studies, which are based on linearized governing equations about a base flow, we use the full nonlinear N-S equations to compute both the base and the disturbed flows. The evolution of the disturbance

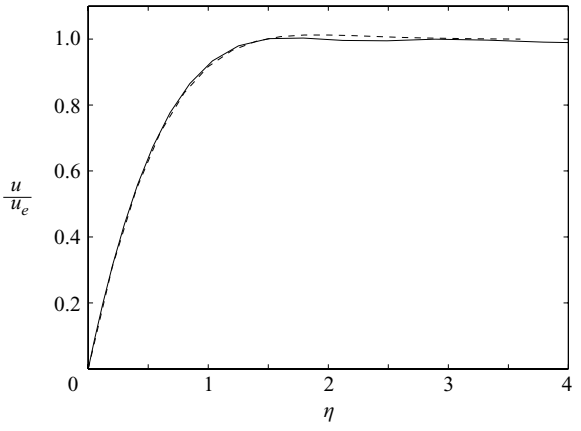

FIGURE 22. Comparison of boundary-layer velocity profile at the leading edge. $Re = 10^5$, $M = 0.15$, $T_w/T_0 = 2.0$, $Pr = 1.0$. ——, computation; – – –, similarity solution.

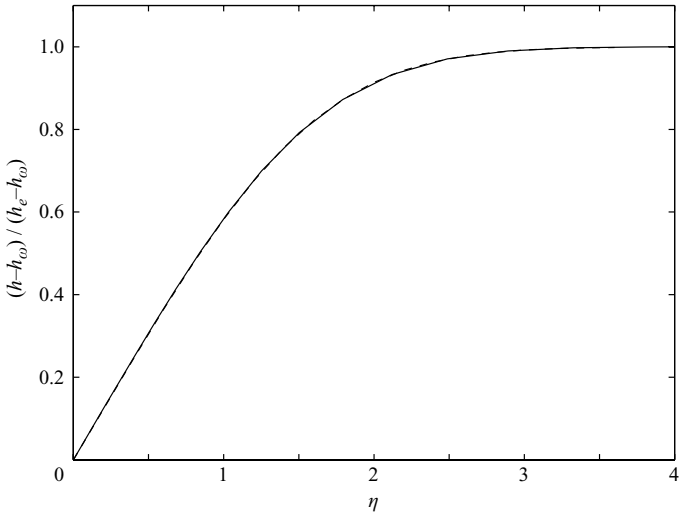

FIGURE 23. As figure 22, but for enthalpy profile.

is obtained by subtracting the base solution from the instantaneous solution. In the present computation, the mean flow is judged to be steady after the residue has dropped by 8 orders of magnitude from its initial value. The mean flow wall vorticity ω_w is shown in figure 24 and it is in very good agreement with those from Collis (1997). In figure 25, the streamwise velocity profile at $x = 2.783$ is shown as a function of the Blasius variable η_b, defined as $\eta_b = y\sqrt{Re/(x+1)}$. Again, the present result agrees well with Collis (1997).

Once the base flow is obtained, acoustic waves are introduced through the inflow sponge at a frequency $\omega = 3.312$ and amplitude $A = 0.001$ (see Xiong 2004 for details). With the mean flow Mach number $M = 0.1$, the downstream acoustic wavelength is $\lambda_a = 20.833$.

The T-S wave field inside the boundary layer induced by the sound wave is plotted in figure 26 using the vertical velocity component. Notice that the overall disturbance

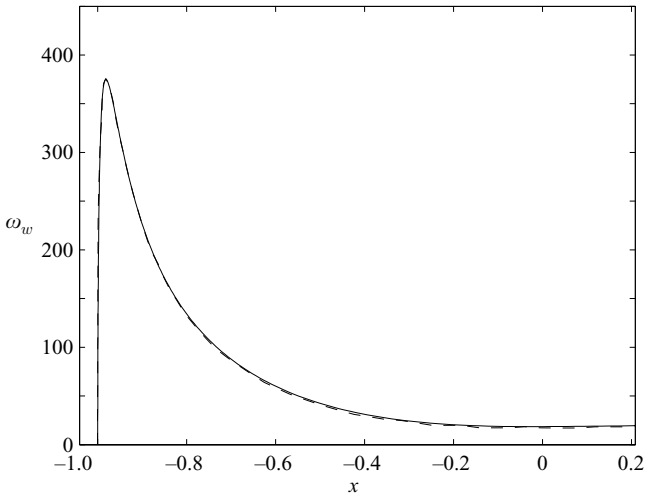

FIGURE 24. Comparison of the wall vorticity ω_w. ——, present computation; – – –, Collis (1997).

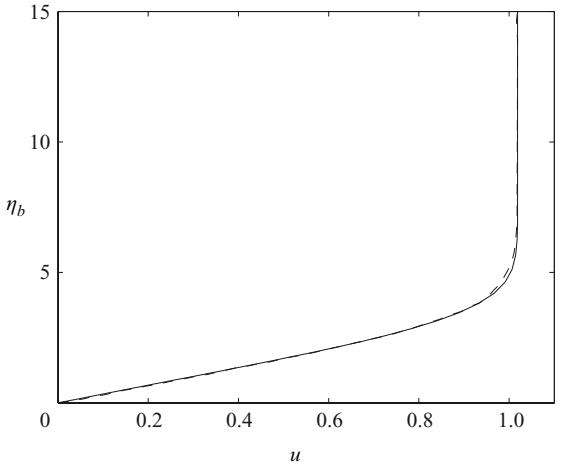

FIGURE 25. Streamwise velocity profile at $x = 2.783$. ——, present computation; – – –, Collis (1997).

flow field in the boundary layer contains not only the excited T-S wave, but also the incoming and scattered acoustic waves.

After subtracting the acoustic components from the total disturbance solution following Wlezien (1994), the amplitude of the T-S wave is shown in figure 27. The results from Lin (1992) (for incompressible flow) and from Collis (1997) are also shown. Again, we can see that the computations have followed similar shapes, with some small quantitative differences. Given the great sensitivity of the growth rate of the T-S wave, the difference is considered to be acceptable, and the overall agreement is satisfactory.

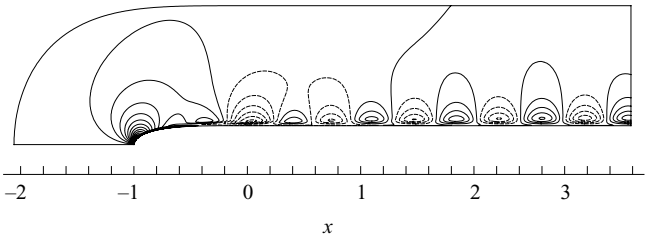

FIGURE 26. Disturbance vertical velocity fields of sound receptivity on a flat plate with a super-ellipse leading edge. Contour levels: $v_{max} = 1.17 \times 10^{-4}$; $v_{min} = -3.90 \times 10^{-4}$; $\Delta v = 8.16 \times 10^{-6}$.

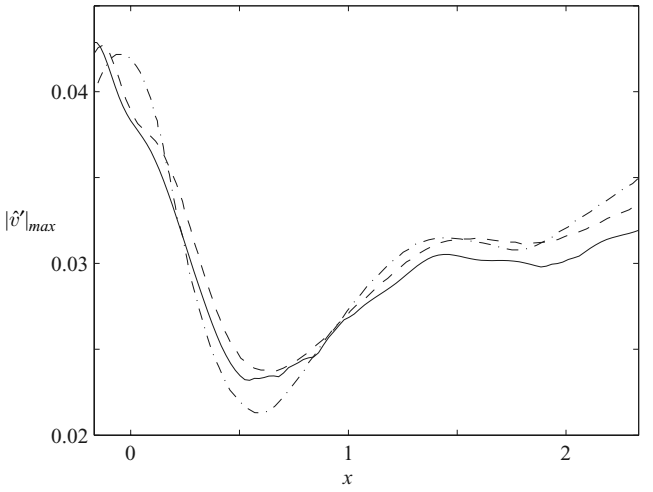

FIGURE 27. Local maximum of the amplitude of the T-S wave based on the vertical disturbance velocity. ——, present computation; – – –, Collis (1997); —·— Lin (1992).

Appendix B. Pressure–strain correlation

Let $\phi_{\alpha\alpha}$ denote the pressure strain correlation (no summation over α) in the equations for $\overline{u^2}$, $\overline{v^2}$ and $\overline{w^2}$,

$$\phi_{\alpha\alpha} = \overline{\frac{p'}{\rho}\frac{\partial u_\alpha}{\partial x_\alpha}}, \tag{B 1}$$

and k and ϵ denote the turbulence kinetic energy and dissipation. Along the stagnation streamline, the $\phi_{\alpha\alpha}$ in the GL, GL-CL and SSG Reynolds stress models takes the following form:

GL model

$$\phi_{11} = -\frac{\epsilon}{k}\left[\alpha_1\left(\overline{u^2} - \tfrac{2}{3}k\right) + 2\alpha_{1w}\overline{u^2}f_n\right] - \frac{\alpha_2}{3}[(2P_{11} - P_{22}) - 2\beta_{2w}(2P_{11} - P_{22})f_n], \tag{B 2}$$

$$\phi_{22} = -\frac{\epsilon}{k}\left[\alpha_1\left(\overline{v^2} - \tfrac{2}{3}k\right) - \alpha_{1w}\overline{u^2}f_n\right] - \frac{\alpha_2}{3}[(2P_{22} - P_{11}) + \beta_{2w}(2P_{11} - P_{22})f_n], \tag{B 3}$$

$$\phi_{33} = -\frac{\epsilon}{k}\left[\alpha_1\left(\overline{w^2} - \tfrac{2}{3}k\right) - \alpha_{1w}\overline{u^2}f_n\right] + \frac{\alpha_2}{3}[(P_{11} + P_{22}) - \beta_{2w}(2P_{11} - P_{22})f_n]. \tag{B 4}$$

GL-CL model

$$\phi_{11} = -\frac{\epsilon}{k}\left[\alpha_1\left(\overline{u^2} - \tfrac{2}{3}k\right) + 2\alpha_{1w}\overline{u^2}f_n\right] - \frac{\alpha_2(2P_{11} - P_{22})}{3} - f_n\left[2(\gamma_{2w} + \gamma'_{2w})P_{11} + 2\gamma_{2w}P_{22} + \frac{2k(2\gamma'_{2w} - \gamma''_{2w})}{3}S_{11}\right], \tag{B 5}$$

$$\phi_{22} = -\frac{\epsilon}{k}\left[\alpha_1\left(\overline{v^2} - \tfrac{2}{3}k\right) - \alpha_{1w}\overline{u^2}f_n\right] - \frac{\alpha_2(2P_{22} - P_{11})}{3} + f_n\left[(\gamma_{2w} + \gamma'_{2w})P_{11} + \gamma_{2w}P_{22} + \frac{k(2\gamma'_{2w} - \gamma''_{2w})}{3}S_{11}\right], \tag{B 6}$$

$$\phi_{33} = -\frac{\epsilon}{k}\left[\alpha_1\left(\overline{w^2} - \tfrac{2}{3}k\right) - \alpha_{1w}\overline{u^2}f_n\right] + \frac{\alpha_2(P_{11} + P_{22})}{3} + f_n\left[(\gamma_{2w} + \gamma'_{2w})P_{11} + \gamma_{2w}P_{22} + \frac{k(2\gamma'_{2w} - \gamma''_{2w})}{3}S_{11}\right]. \tag{B 7}$$

where

$$P_{11} = -\overline{u^2}\,\frac{\partial U}{\partial x}, \quad P_{22} = -\overline{v^2}\,\frac{\partial V}{\partial y}, \quad S_{11} = \frac{\partial U}{\partial x}, \quad S_{22} = \frac{\partial V}{\partial y}, \quad f_n = \frac{k^{3/2}}{\alpha_n \epsilon x_n}. \tag{B 8}$$

The coefficients are $\alpha_1 = 1.8$, $\alpha_2 = 0.6$, $\alpha_{1w} = 0.5$, $\beta_{2w} = 0.3$, $\gamma_{2w} = 0.08$, $\gamma'_{2w} = 0.1$, $\gamma''_{2w} = 0.4$, $\alpha_n = 2.5$. The x_n is the normal distance to the wall.

SSG model

$$\phi_{11} = -(\sigma_1\epsilon + \sigma_1^* P)b_{11} + \sigma_2\epsilon\left(b_{11}^2 - \tfrac{1}{3}\Pi_b\right) + \left(\sigma_3 - \sigma_3^*\Pi_b^{1/2}\right)kS_{11} + \tfrac{2}{3}\sigma_4 k(2b_{11}S_{11} - b_{22}S_{22}), \tag{B 9}$$

$$\phi_{22} = -(\sigma_1\epsilon + \sigma_1^* P)b_{22} + \sigma_2\epsilon\left(b_{22}^2 - \tfrac{1}{3}\Pi_b\right) + \left(\sigma_3 - \sigma_3^*\Pi_b^{1/2}\right)kS_{22} + \tfrac{2}{3}\sigma_4 k(2b_{22}S_{22} - b_{11}S_{11}), \tag{B 10}$$

$$\phi_{33} = -(\sigma_1\epsilon + \sigma_1^* P)b_{33} + \sigma_2\epsilon\left(b_{33}^2 - \tfrac{1}{3}\Pi_b\right) - \tfrac{2}{3}\sigma_4 k(b_{11}S_{11} + b_{22}S_{22}), \tag{B 11}$$

where

$$P = P_{11} + P_{22}, \qquad b_{ii} = \frac{\overline{u_i u_i}}{2k} - \tfrac{1}{3}, \qquad \Pi_b = b_{ii}^2. \tag{B 12}$$

The coefficients are $\sigma_1 = 3.4$, $\sigma_1^* = 1.8$, $\sigma_2 = 4.2$, $\sigma_3 = 0.8$, $\sigma_3^* = 1.3$, $\sigma_4 = 1.25$.

REFERENCES

Ames, F. E. & Moffat, R. J. 1990 Heat transfer with high intensity, large scale turbulence: The flat plate turbulent boundary layer and the cylindrical stagnation point. In *Dept of Mech. Engng Rep.* HMT-44. Stanford University, Stanford, CA.

Bae, S., Lele, S. K. & Sung, H. J. 2000 Influence of inflow disturbances on stagnation-region heat transfer. *Trans. ASMEC: J. Heat Transfer* **122**, 258–265.

Bardina, J., Huang, P. G. & Coakley, T. J. 1997 Turbulence modeling validation. *AIAA Paper* 97-2121.

Carnevale, G. F. Velasco Fuentes, O. U. & Orlandi, P. 1997 Inviscid dipole-vortex rebound from a wall or coast. *J. Fluid Mech.* **351**, 75–103.

Champion, M. & Libby, P. A. 1991 Asymptotic analysis of stagnating turbulent flows. *AIAA J.* **29**, 16–24.

Champion, M. & Libby, P. A. 1994 Reynolds stress description of opposed and impinging turbulent jets II. Axisymmetric jets impinging on nearby walls. *Phys. Fluids* **6** (5), 1805–1819.

Collis, S. S. 1997 A computational investigation of receptivity in high-speed flow near a swept leading-edge. PhD thesis, Stanford University.

Craft, T. J., Graham, L. J. W. & Launder, B. E. 1993 Impinging jet studies for turbulence model assessment II. An examination of the performance of four turbulence models. *Intl J. Heat Mass Transfer* **36** (10), 2685–2697.

Dullenkopf, K. & Mayle, R. E. 1995 An account of free-stream-turbulence length scale on laminar heat transfer. *Trans. ASME J. Turbomachinary* **117**, 401–406.

Durbin, P. 1996 On the $k-\epsilon$ stagnation point anomaly. *Intl J. Heat and Fluid Flow* **17**, 89–90.

Eiseman, P. 1985 Grid generation for fluid mechanics. *Annu. Rev. Fluid Mech.* **17**, 487–522.

Gibson, M. M. & Launder, B. E. 1978 Ground effects on pressure fluctuation in the atmospheric boundary layer. *J. Fluid Mech.* **86**, 491–591.

Giedt, W. H. 1949 Investigation of variation of point unit heat transfer coefficient around a cylinder normal to an airstream. *Trans. ASME* **71**, 375–381.

Görtler, H. 1955 Three dimensional instability of the plane stagnation flow with respect to vortical disturbance. In *Fifty Years of Boundary Layer Research* (ed. H. Görtler & W. Tollmien), pp. 304–314. Vieweg.

Hämmerlin, G. 1955 On instability theory of plane stagnation point flow. In *Fifty Years of Boundary Layer Research* (ed. H. Görtler & W. Tollmien), pp. 315–327. Vieweg.

Hegge-Zijnen, B. G. V. D. 1957 Heat transfer from horizontal cylinders to a turbulent air flow. *Appl. Sci. Res.* A **7**, 205–223.

Hiemenz, K. 1911 Die Grenzschicht an einem in den gleichförmigen Flüssigkeitstorm eingetauchten geraden Kieiszylinder. Thesis, Göltingen, *Dingl. Polytech. J.* **326**, 321–324.

Hunt, J. C. R. 1973 A theory of turbulent flow round two-dimensional bluff bodies. *J. Fluid Mech.* **61**, 625–706.

Im, Y. H., Huh, K. Y. & Kim, K.-Y. 2002 Analysis of impinging and countercurrent stagnating flows by Reynolds stress model. *Trans. ASMEI: J. Fluids Engng* **124**, 706–718.

Ishigaki, M. 1970 Periodic boundary layer near a two-dimensional stagnation point. *J. Fluid Mech.* **43**, 477–486.

Kestin, J. & Wood, R. T. 1970 On the stability of two-dimensional stagnation flow. *J. Fluid Mech.* **44**, 461–479.

Kestin, J. & Wood, R. T. 1971 The influence of turbulence on mass transfer from cylinders. *Trans. ASMEC: J. Heat Transfer* **93**, 321–327.

Kestin, J., Maeder, P. F. & Sogin, H. H. 1961 The influence of turbulence on the trnafer of heat to cylinders near the stagnation point. *Z. Angew. Math. Phys.* **12**, 115–132.

Lee, M. J. & Reynolds, W. C. 1985 Numerical experiments on the structure of homogeneous turbulence. *TF Rep.* 24. Stanford University.

Lighthill, M. J. 1954 The response of laminar skin friction and heat transfer to fluctuations in the stream velocity. *Proc. R. Soc. Lond.* A **224**, 1–23.

Lin, N. 1992 Receptivity of the boundary layer over a flat plate with different leading-edge geometries: numerical simulations. PhD thesis, Arizona State University.

Lin, R. S. & Malik, M. R. 1996 On the stability of attachment-line boundary layers. Part 1. The incompressible swept Himenz flow. *J. Fluid Mech.* **311**, 239–255.

Lowery, G. W. & Vachon, R. I. 1975 Effect of turbulence on heat transfer from heated cylinders. *Intl J. Heat Mass Transfer* **18**, 1229–1242.

Lui, C. 2003 A numerical investigation of shock associated noise. PhD thesis, Stanford University.

Lyell, M. J. & Huerre, P. 1985 Linear and nonlinear stability of plane stagnation flow. *J. Fluid Mech.* **161**, 295–312.

Medic, G. & Durbin, P. A. 2002 Toward improved prediction of heat transfer on turbine blades. *Trans. ASME J. Turbomachinery* **124**, 187–192.

Mehendale, A. B., Han, J. C. & Ou, S. 1991 Influence of high mainstream turbulence on leading edge heat transfer. *Trans. ASMEC: J. Heat Transfer* **113**, 843–850.

Merchant, G. J. & Davis, S. H. 1989 Modulated stagnation-point flow and steady streaming. *J. Fluid Mech.* **198**, 543–555.

Moin, P., Squires, K., Cabot, W. & Lee, S. 1991 A dynamic subgrid-scal model for compressible turbulence and scalar transport. *Phys. Fluids* A **3** (11), 2746–2757.

Morkovin, M. V. 1969 Bypass-transition research: issues and philosophy. *Tech. Rep.* AFFDL-TR-68-149. Air Force Flight Dynamics laboratory, Wright–Paterson Air Force Base.

Morkovin, M. V. 1979 On the question of instabilities upstream of cylindrical bodies. *NASA Contractor Rep.* 3231.

Orlandi, P. 1990 Vortex dipole rebound from a wall. *Phys. Fluids* A **2**, 1429–1436.

Pedley, T. J. 1972 Two-dimensional boundary layers in a free stream which oscillates without reversing. *J. Fluid Mech.* **55**, 359–383.

Piercy, N. A. V. & Richardson, E. G. 1928 The variation of velocity amplitude close to the surface of a cylinder moving through a viscous fluid. *Phil. Mag. Ser. 7*, **6**, 970–977.

Piercy, N. A. V. & Richardson, E. G. 1930 The turbulence in front of a body moving through a viscous fluid. *Phil. Mag. Ser. 7*, **9**, 1038–1041.

Pope, S. B. 2000 *Turbulen Flows*. Cambridge University Press.

Reshotko, E. & Beckwith, I. E. 1957 Compressible laminar boundary layer over a yawed infinite cylinder with heat transfer and arbitrary Prandtl number. 1379. NACA Rep.

Smith, M. C. & Kuethe, A. M. 1966 Effects of turbulence on laminar skin friction and heat transfer. *Phys. Fluids* **9** (12), 2337–2344.

Spalart, P. R. 1989 Direct numerical study of leading-edge contamination. *AGARDC* **438** (5.1–5.13), 457–468.

Spalart, P. R. & Allmaras, S. R. 1992 A one-equation turbulence model for aerodynamic flows. *AIAA Paper* 92-0439.

Speziale, C. G., Sarkar, S. & Gatski, T. B. 1991 Modelling the pressure–strain correlation of turbulence: an invariant dynamic systems approach. *J. Fluid Mech.* **227**, 245–272.

Sutera, S. P. 1965 Vorticity amplification in staganation-point flow and its effect on heat transfer. *J. Fluid Mech.* **21**, 513–534.

Theofilis, V., Fedorov, A., Obrist, D. & Dallmann, U. C. 2003 The extended Görtler–Hämmerlin model for linear instability of three-dimensional incompressible swept attachment-line boundary layer flow. *J. Fluid Mech.* **487**, 271–313.

Van Fossen, G. J., Simoneau, R. J. & Ching, C. Y. 1995 Influence of turbulence parameters, Reynolds number and body shape on stagnation region heat transfer. *Trans. ASMEC: J. Heat Transfer* **117**, 593–603.

Wilcox, D. C. 2001 Turbulence modeling: an overview. *AIAA Paper* 2001-0724.

Wilson, S. D. R. & Gladwell, I. 1978 The stability of a two-dimensional stagnation flow to three-dimensional disturbances. *J. Fluid Mech.* **84**, 517–527.

Wlezien, R. W. 1994 Measurement of acoustic receptivity. *25th AIAA Fluid Dyn. Conf. AIAA Paper* 94-2221.

Xiong, Z. 2004 Stagnation point flow and heat transfer under free-stream turbulence. PhD thesis, Stanford University.

Xiong, Z. & Lele, S. K. 2001 Numerical study of leading-edge heat transfer under free-stream turbulence. *AIAA Paper* 2001-1016.

Xiong, Z. & Lele, S. K. 2004 Distortion of upstream disturbances in a Hiemenz boundary layer. *J. Fluid Mech.* **519**, 201–232.

Xiong, Z., Nagarajan, S. & Lele, S. K. 2004 Simple method for generating inflow turbulence. *AIAA J.* **42**, 2164–2166.